frontiers | Frontiers in Energy Research

TYPE Review
PUBLISHED 29 September 2022
DOI 10.3389/fenrg.2022.979573

OPEN ACCESS

EDITED BY
Andreas Busch,
Heriot-Watt University, United Kingdom

REVIEWED BY
Jiaqi Wang,
Harbin Engineering University, China
Marwan Fahs,
National School for Water and Environmental Engineering, France

*CORRESPONDENCE
J. Carlos Santamarina,
carlos.santamarina@kaust.edu.sa

SPECIALTY SECTION
This article was submitted to Carbon Capture, Utilization and Storage, a section of the journal Frontiers in Energy Research

RECEIVED 27 June 2022
ACCEPTED 15 August 2022
PUBLISHED 29 September 2022

CITATION
Liu Q, Benitez MD, Xia Z and Santamarina JC (2022), Pore-scale phenomena in carbon geological storage (Saline aquifers—Mineralization—Depleted oil reservoirs).
Front. Energy Res. 10:979573.
doi: 10.3389/fenrg.2022.979573

Pore-scale phenomena in carbon geological storage (Saline aquifers—Mineralization—Depleted oil reservoirs)

Qi Liu, Marcelo D. Benitez, Zhao Xia and J. Carlos Santamarina*

KAUST King Abdullah University of Science and Technology, Thuwal, Saudi Arabia

The injection of CO_2 into geological formations triggers inherently coupled thermo-hydro-chemo-mechanical processes. The reservoir pressure and temperature determine the CO_2 density, the CO_2-water interfacial tension, and the solubility of CO_2 in water (hindered by salts and competing gases). The CO_2-water interface experiences marked pinning onto mineral surfaces, and contact angles can range from the asymptotic advancing to receding values, in contrast to the single contact angle predicted by Young's equation. CO_2 dissolves in water to form carbonic acid and the acidified water dissolves minerals; mineral dissolution enhances porosity and permeability, triggers settlement, may couple with advection to form "wormholes", produces stress changes and may cause block sliding and shear bands. Convective currents can emerge beneath the CO_2 plume and sustain CO_2 and mineral dissolution processes. On the other hand, mineralization is a self-homogenizing process in advective regimes. The crystallization pressure can exceed the tensile capacity of the host rock and create new surfaces or form grain-displacive lenses. Within the rock matrix, coupled reactive-diffusion-precipitation results in periodic precipitation bands. Adequate seal rocks for CO_2 geological storage must be able to sustain the excess capillary pressure in the buoyant CO_2 plume without experiencing open-mode discontinuities or weakening physico-chemical interactions. CO_2 injection into depleted oil reservoirs benefits from time-proven seals; in addition, CO_2 can mobilize residual oil to simultaneously recover additional oil through oil swelling, ganglia destabilization, the reduction in oil viscosity and even miscible displacement. Rapid CO_2 depressurization near the injection well causes cooling under most anticipated reservoir conditions; cooling can trigger hydrate and ice formation, and reduce permeability. In some cases, effective stress changes associated with the injection pressure and cooling thermoelasticity can reactivate fractures. All forms of carbon geological storage will require large reservoir volumes to hold a meaningful fraction of the CO_2 that will be emitted during the energy transition.

KEYWORDS

porous media, carbon geological storage, dissolution, mineralization, oil recovery, thermal effect, seals

Introduction

We emit ~40 billion tons of CO_2 per year, however, emissions should decrease to ≤18 billion tons per year to prevent further global warming (IPCC, 2021). This scenario will require reduced fossil fuel consumption and CO_2 capture and geological storage. Currently, the total capacity of operating CO_2 storage facilities is 150 million tons/year (GCCSI, 2021), i.e., three orders of magnitude lower than needed. Therefore, thousands of new geological storage projects must come online in the near future.

The injection of CO_2 into geological formations triggers inherently coupled thermo-hydro-chemo-mechanical processes. In this manuscript, we present a comprehensive review of the underlying physical processes, summarize the properties of bulk phases and interfaces, and analyze the most relevant pore-scale phenomena that can affect the long-term geological storage of CO_2.

CO_2 and aqueous solutions: Properties and interactions

Fluids involved in carbon geological storage exhibit different pressure and temperature-dependent bulk properties, solubilities and capillary response.

Density

The pressure and temperature-dependent CO_2 density determines storage capacity, gravity-driven displacement, instabilities, and capillary pressure against the seal (Van der Meer, 1993; DiCarlo, 2013). Figure 1 shows the density ρ [kg/m^3] of water, oil and CO_2 as a function of pressure and temperature: the density of CO_2 varies significantly but remains a buoyant phase, while water is the heavier fluid in high-temperature reservoirs.

Geological storage projects can involve gas, liquid and supercritical CO_2 (Figure 2). The gas-liquid phase boundary $P = 0.0008(\frac{T}{^\circ C})^2 + 0.1(\frac{T}{^\circ C}) + 3.5$ MPa applies until the critical point (T = 31°C and P = 7.37 MPa).In the supercritical regime, beyond the critical point, the Widom line divides the lighter gaseous-like regime from the denser liquid-like regime (Simeoni et al., 2010; Houben et al., 2021). Density gradients in P or T are pronounced across the Widom line, particularly near the critical point; for example, the CO_2 density changes from 661 kg/m^3 to 285 kg/m^3 when the temperature increases from 35°C to 50°C at a constant pressure of P = 8.5 MPa (see Figure 2).

Viscosity

Liquid CO_2 and water are Newtonian fluids, yet most crude oils exhibit some shear thinning. Figure 3 shows the reduction in viscosity μ [μPa·s] with temperature for different types of crude oils, water and CO_2 (Note: viscosity shown in log-scale). Molecular vibration acts against intermolecular attraction hence the viscosity of liquids decreases with higher temperature while pressure has a second-order effect. On the other hand, the viscosity of gases tends to increase with temperature and pressure because the collision frequency increases. The viscosity of CO_2 is much lower than water and oil, and it experiences sharp changes across the liquid-gas LG phase boundary and the Widom line WL in agreement with density changes.

Interfacial tension

Interfacial tension γ [mN/m] and contact angle θ [°] determine capillary phenomena between multiphase fluids in porous media. The capillary pressure ΔP is the pressure difference between the non-wetting P_{nw} [Pa] and the wetting P_w [Pa] fluid; for a spherical interface of radius r [m]

$$P_{nw} - P_w = P_c = \frac{2\gamma \cdot \cos\theta}{r} \quad (1)$$

The interfacial tension between CO_2 and water is reported as a function of pressure and temperature in most cases. However, intermolecular distance l_0 [m] determines molecular interaction at the interface, therefore the CO_2 density ρ [kg/m^3] which scales as $\rho \propto l_0^{-3}$ is a more meaningful parameter to predict the interfacial tension. Figure 4 plots compiled CO_2-water interfacial tension data gathered from the literature and our own studies as a function of CO_2 density (computed from reported pressure and temperature conditions): there is a clear decrease in the interfacial tension with increasing CO_2 density. The remaining spread in the data indicates that thermal vibration affects interfacial tension beyond its role on density(in addition to measurement variability among devices and test protocols).

Wettability—contact angles

Wettability captures the interaction between two fluids and the mineral surface. Wettability plays a critical role in capillary phenomena, pore-scale fluid arrangement, and macroscopic multiphase flow in CO_2 geological storage.

Contact angle measurements provide an apparently simple assessment of the otherwise complex physical processes that

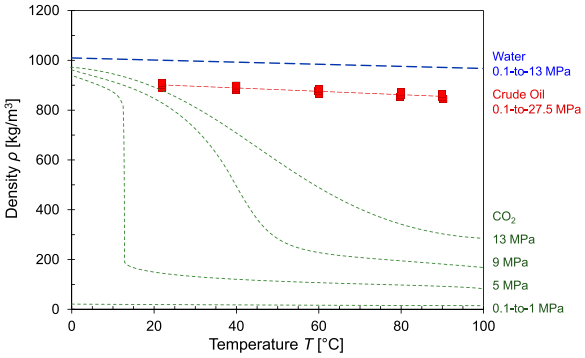

FIGURE 1
Density as a function of pressures and temperature: water, crude oil and CO_2. Data sources: Karnanda et al., 2013, NIST Chemistry WebBook., 2022, Freund et al., 2006.

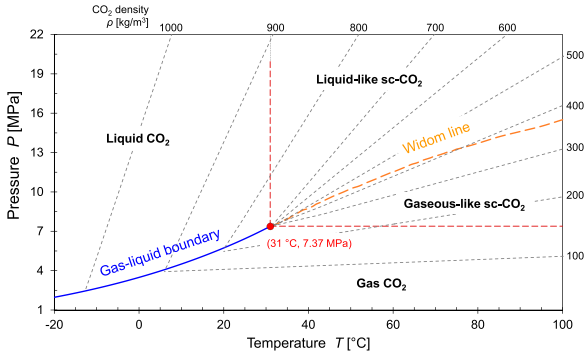

FIGURE 2
Carbon dioxide phase diagram. Note that there are marked changes across the Widom line within the supercritical regime. Data for density lines: Bachu., 2003.

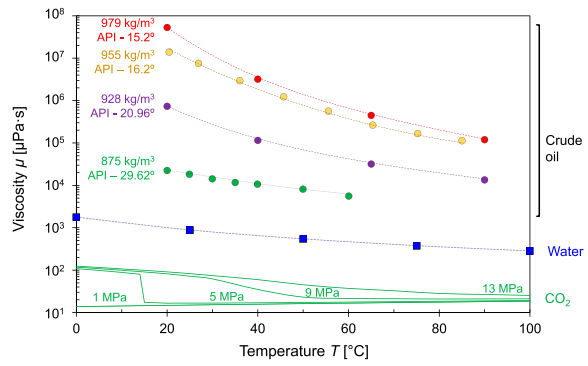

FIGURE 3
Viscosity as a function of temperature: various crude oils (●), water (■) and CO_2 (continue lines - different pressures). Crude oils include heavy (density ρ = 979 kg/m^3, 955 kg/m^3), medium (ρ = 928 kg/m^3) and light oils (ρ = 875 kg/m^3). Data sources: water: Schmelzer et al. (2005), crude oil: Gachuz-Muro and Sohrabi., 2013, Akhmadiyarov et al., 2019 and CO_2: NIST Chemistry WebBook., 2022.

underline wettability (Sargent et al., 2005; Drelich et al., 2020). Force equilibrium parallel to the mineral surface relates the contact angle to the interfacial tensions γ [N/m] between the fluid F, liquid L and solid S (Young, 1805):

$$\sum F_H = (\gamma_{FS} - \gamma_{LS}) - \gamma_{LF}\cos\theta \quad (2)$$

On the other hand, force equilibrium normal to the substrate surface allows us to anticipate the adhesion A [N/m] between the liquid-fluid interface and the mineral substrate $A = \gamma_{LF}\sin\theta$. Equilibrium contact angle measurements show that both calcite and quartz are strongly water-wet (Figure 5, Bikkina, 2011; Arif et al., 2017a).

In contrast to the single thermodynamic contact angle predicted by Young's equation, interfaces can exhibit a range of contact angles between two asymptotic values: the advancing contact angle θ_A and the receding contact angle θ_R when it is measured in a quasi-static condition. For example, a deionized water droplet resting on a horizontal smooth calcite surface surrounded by supercritical CO_2 at P = 9 MPa and T = 40°C forms an advancing contact angle θ_A = 138° and a receding contact angle θ_R =20° (quasi-static injection/extraction measurements conducted for this study). Even dynamic measurements show marked hysteresis; for example, a water droplet released on a smooth calcite surface in a CO_2 environment at P = 20 MPa and T = 35°C exhibits an advancing contact angle θ_A = 122° and a receding contact angle θ_R =108° (see inset in Figure 5—Note: dynamic contact angle measurements based on a sliding droplet do not capture the full pinning effect of the contact line measured in quasi-static tests at the verge of sliding, thus, hysteresis in dynamic tests is smaller than in quasi-static tests—Huhtamäki, et al., 2018).

X-ray CT measurements confirm these observations and show that a wide range of contact angles exist *in-situ* possibly due to (Andrew et al., 2014): 1) the contact line adhesion A, 2) surface roughness and chemical inhomogeneities on the solid surface (de Gennes, 1985; Eral et al., 2013), and 3) the fact that *in-situ* contact angles rarely represent equilibrium conditions.

Let's modify Young's force equilibrium analysis parallel to the mineral surface to take into consideration the adhesion force A acting against both advancing on receding directions; then the anticipated contact angle hysteresis is $\cos\theta_R - \cos\theta_A = 2A/\gamma_{LF}$. Conversely, we can recover the adhesion force from contact angle hysteresis measurements $A = \gamma_{LF}(\cos\theta_R - \cos\theta_A)/2$. Evidently, the adhesion force scales with the liquid-fluid interfacial tension γ_{LF} and should not be ignored in wettability analyses. For example, consider the water-CO_2-calcite system reported above: the computed adhesion force A = 18.8 mN/m while the

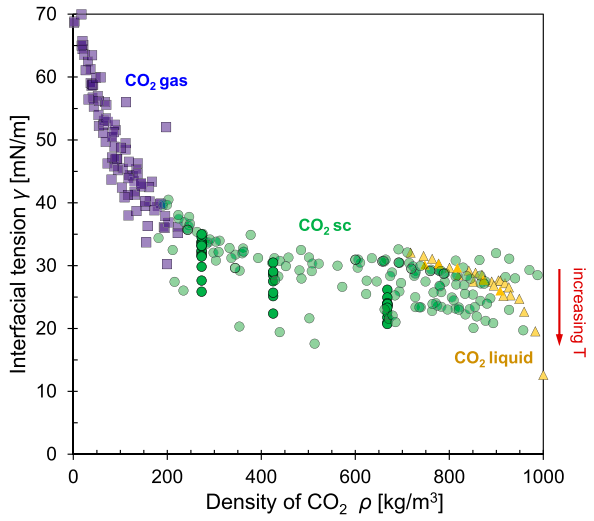

FIGURE 4
The interfacial tension between CO_2 and water as a function of CO_2 density. The dataset combines results for CO_2 in gas (■), super critical (●) and liquid states (▲). Note: density determines molecular proximity for electrical interactions, thus, it emerges as the governing variable. Still, the data spread is due to thermal effects: interfacial tension decreases with increased random vibration. Data sources: Hough et al., 1952, Park et al., 2005, Sutjiadi-Sia et al., 2008, Chun and Wilkinson., 1995, Da Rocha et al., 1999, Hebach et al., 2002, Chiquet et al., 2007, Kvamme et al., 2007, Espinoza and Santamarina., 2010, Georgiadis et al., 2010, and measurements by the authors for this study (2022).

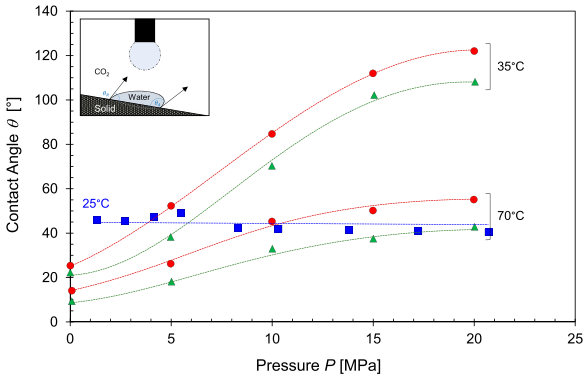

FIGURE 5
Contact angle formed by a water droplet on calcite in a CO_2 atmosphere as function of CO_2 pressure. Advancing contact angle (●), receding contact angle (▲) and static contact angle (■). Data sources: Bikkina, 2011, Arif et al., 2017a. For clarity, only a subset of the dataset is presented in this figure.

water-CO_2 interfacial tension is γ_{LF} = 22.39 mN/m (θ_A = 138°, θ_R =20°).

CO_2 solubility in aqueous solutions

While two phases may exhibit interfacial tension, their mutual solubilities can have important implications. For example, CO_2 dissolves in water and enhances carbon geological storage, on the other hand, minerals dissolve in CO_2-acidified water and may trigger internal instabilities (details follow).

The solubility of CO_2 in water increases with pressure but decreases with temperature. Henry's law relates solubility χ [mol/l] to the partial pressure of CO_2 P_{CO2} [kPa] through the temperature dependent Henry's constant k_H [mol L^{-1} kPa^{-1}]:

$$\chi_{CO_2} = k_H P_{CO_2} \quad (3)$$

where k_H = 3.4 × 10^{-4} [mol L^{-1} kPa^{-1}] at temperature T = 298.15 K. Figure 6A shows the evolving CO_2 solubility in water as a function of pressure for different temperatures.

CO_2 dissolves in water to form aqueous carbon dioxide CO_2 (aq). The ionization of carbonic acid produces H^+ and decreases the pH:

$$CO_2(g) \Leftrightarrow CO_2(aq) \quad (4)$$

$$CO_2(aq) + H_2O \Leftrightarrow H_2CO_3 \quad \mathrm{Log}\,K_{25°C} = -8.23 \quad (5)$$

$$H_2CO_3 \Leftrightarrow H^+ + HCO_3^- \quad \mathrm{Log}\,K_{25°C} = -6.38 \quad (6)$$

$$HCO_3^- \Leftrightarrow H^+ + CO_3^{2-} \quad \mathrm{Log}\,K_{25°C} = -10.48 \quad (7)$$

Therefore, the equilibrium pH for water with dissolved CO_2 is also a function of pressure and temperature (Figure 6B).

Effect of salinity

High salinity is a common condition in reservoirs considered for CO_2 geological storage, such as saline aquifers, depleted hydrocarbon reservoirs and coalbeds. In general, CO_2 solubility in water may either increase (salting-in effect, e.g. $NaClO_4$ and K_3PO_4) or decrease (salting-out effect, e.g., salts from strong bases and strong acids such as NaCl, $CaCl_2$ and $MgCl_2$ (Yasunishi and Yoshida 1979; García, 2005; García et al., 2005). In most geological settings, CO_2 solubility decreases with salt concentration as water mobility decreases, particularly for small high-valence ions. Consequently, the CO_2 solubility in salt solutions at the same ionic concentration follows the following sequence: highest in KCl solutions → NaCl → $CaCl_2$ → lowest in $MgCl_2$ solutions. Figure 7 shows that the solubility of CO_2 decreases by ~50% for a 3 mol NaCl solution compared to deionized water. Therefore, the storage capacity for dissolved CO_2 decreases by half and the needed reservoir size doubles in brine saturated formations.

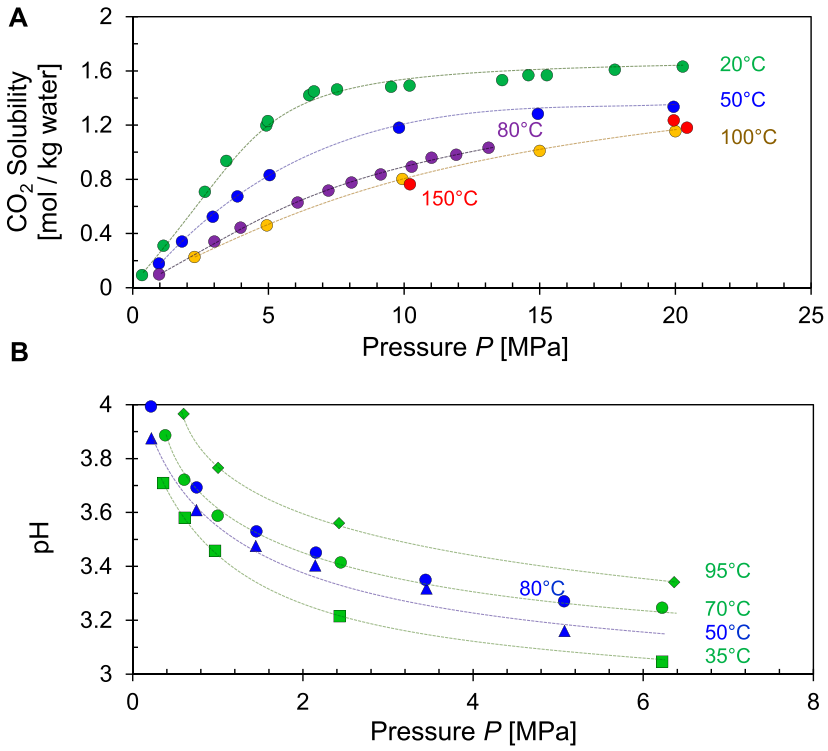

FIGURE 6
Solubility of CO_2 in water and change in pH. **(A)** CO_2 solubility increases with pressure but decreases with temperatures—Data sources: Duan and Sun., 2003, Sanaei et al., 2019. **(B)** Equilibrium pH for CO_2 saturated water as a function of pressure and temperatures—Data sources: blue = Haghi et al., 2017; green = Peng et al., 2013.

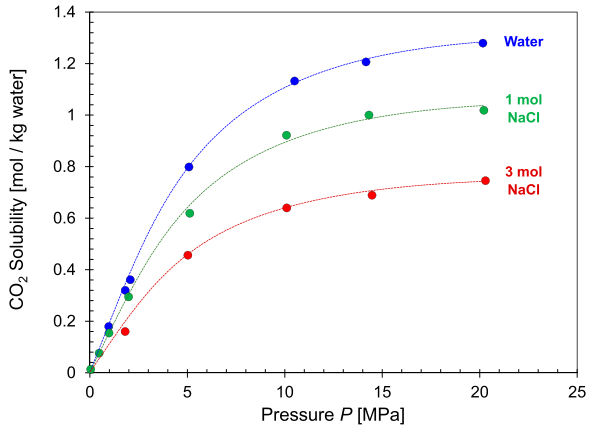

FIGURE 7
The effect of salinity on CO_2 solubility in NaCl solutions as a function of pressures (T = 50°C—Data source: Koschel et al., 2006). Data at p = 101.3 kPa were gathered at T = 25°C thus solubility values are higher than the rest of the trend for T = 50°C (Data sources: Markham and Kobe., 1941; Koschel et al., 2006; Duan et al., 2006; Kiepe et al., 2002).

Effect of mixed gases

Flue gas released at power plants and industrial sources contains N_2 (~66%), CO_2 (10%–15%), water vapor, other gases such as SO_2, H_2S, NO_2, and light hydrocarbons such as CH_4 (Bell et al., 2021). Separation is costly and the presence of competing gases affects the solubility of CO_2 in water mainly because: (1) the solubility of CO_2 in water depends on its partial pressure which decreases in a mixed gas at constant total pressure, and (2) competing ions. In the case of a N_2-CO_2-water system, N_2 does not react with water, therefore the solubility of CO_2 only depends on its partial pressure or mole fraction in the mixed gas (Figure 8A).

Similar to salt, coexisting gases can either promote or inhibit CO_2 solubility, yet competition is more common in carbon storage. For example, the dissolution of SO_2 in water involves the following reactions (Goldberg and Parker., 1985):

$$SO_2 + H_2O \rightleftharpoons H_2SO_3 \quad (8)$$

$$H_2SO_3 \rightleftharpoons H^+ + HSO_3^- \quad (9)$$

$$HSO_3^- \rightleftharpoons H^+ + SO_3^{2-} \quad (10)$$

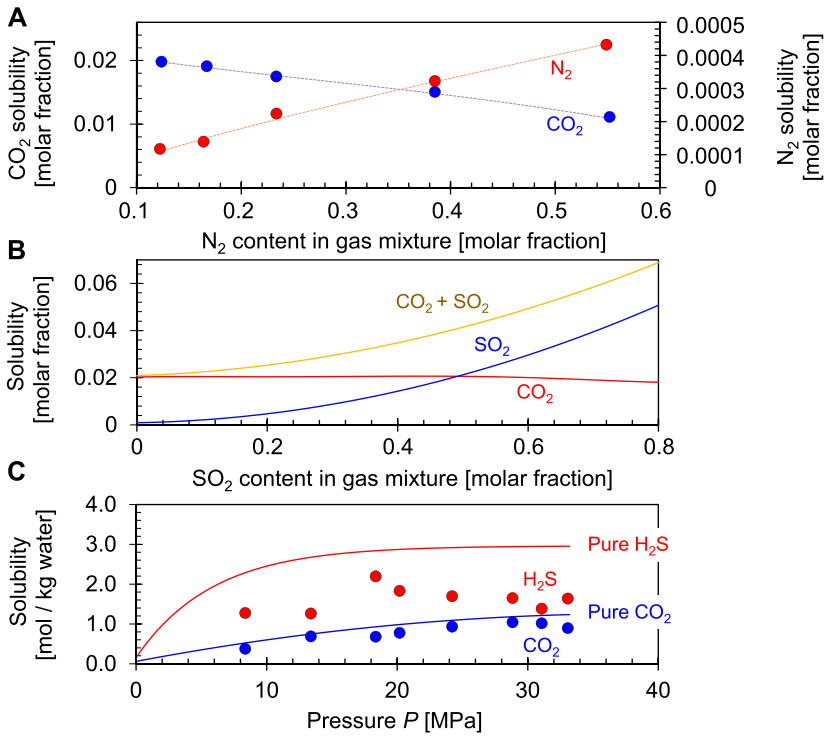

FIGURE 8
Effects mixed gas of CO_2 solubility. **(A)** CO_2 and N_2 solubilities in the N_2+CO_2+H_2O systems at a T = 34.85°C and p = 8.0 MPa. Data source: Nakhaei-Kohani et al., 2022. **(B)** CO_2 and SO_2 solubilities in the SO_2+CO_2+H_2O systems at a T = 50°C and p = 10 MPa. Data source: Miri et al., 2014. **(C)** CO_2 and H_2S solubilities in the H_2S + CO_2+H_2O systems at a T = 120°C. Trends and data from Savary et al., 2012.

$$2HSO_3^- \rightleftharpoons S_2O_5^{2-} + H_2O \quad (11)$$

The generated H^+ competes with the ionization of carbonic acid and decreases the CO_2 solubility (Figure 8B). Similarly, H_2S dissolution in water inhibits CO_2 dissolution as well (Figure 8C):

$$H_2S + H_2O \rightleftharpoons H^+ + HS^- \quad (12)$$

$$HS^- + H_2O \rightleftharpoons H^+ + S^{2-} \quad (13)$$

Fluid-Mineral interaction: Dissolution and precipitation

Water acidifies in the presence of CO_2 and prompts mineral dissolution. The consequences of reactive fluids on the reservoir and seal stability require careful consideration.

Mineral dissolution in CO_2 acidified water

A mineral's crystal structure determines its susceptibility to dissolution in CO_2 acidified water. In particular, crystallographic orientation may cause spatially heterogeneous dissolution (Daval et al., 2013; Pollet-Villard et al., 2016; Oelkers et al., 2018).

Crystal structure

Silicates and carbonates are the most common minerals in CO_2 geological reservoirs. Others, minerals include oxides, sulfides, sulfate and halide.

Silicates are abundant and chemically reactive with carbonated water, thus, they have become the most promising mineral class for carbon mineralization (O'Connor et al., 2002). The fundamental unit in silicate structures is the silicon-oxygen tetrahedron $(SiO_4)^{4-}$ (see Figure 9A). Metal ions are present in all silicates except quartz. Other cations with similar dimensions such as Al^{3+}, Mg^{2+}, Fe^{2+}, Fe^{3+}, Mn^{2+} and Ti^{4+} can replace Si^{4+} from tetrahedral groups by isomorphic substitution (Brigatti et al., 2006).

Carbonates are common in most formations currently considered for CO_2 geological storage. The carbonate ion (CO_3^{2-}) is the basic structural unit of carbonate minerals (see Figure 9B). This anion forms ionic bonds with cations such as Ca^{2+}, Mg^{2+}, Fe^{2+}, Mn^{2+} as well as rare-earth elements e.g., Ba^{2+}, Ce^{3+}. Calcite $CaCO_3$, magnesite $MgCO_3$, rhodochrosite $MnCO_3$, siderite $FeCO_3$, and dolomite $CaMg(CO_3)_2$ are some of the most common carbonate minerals in nature (Effenberger et al., 1981).

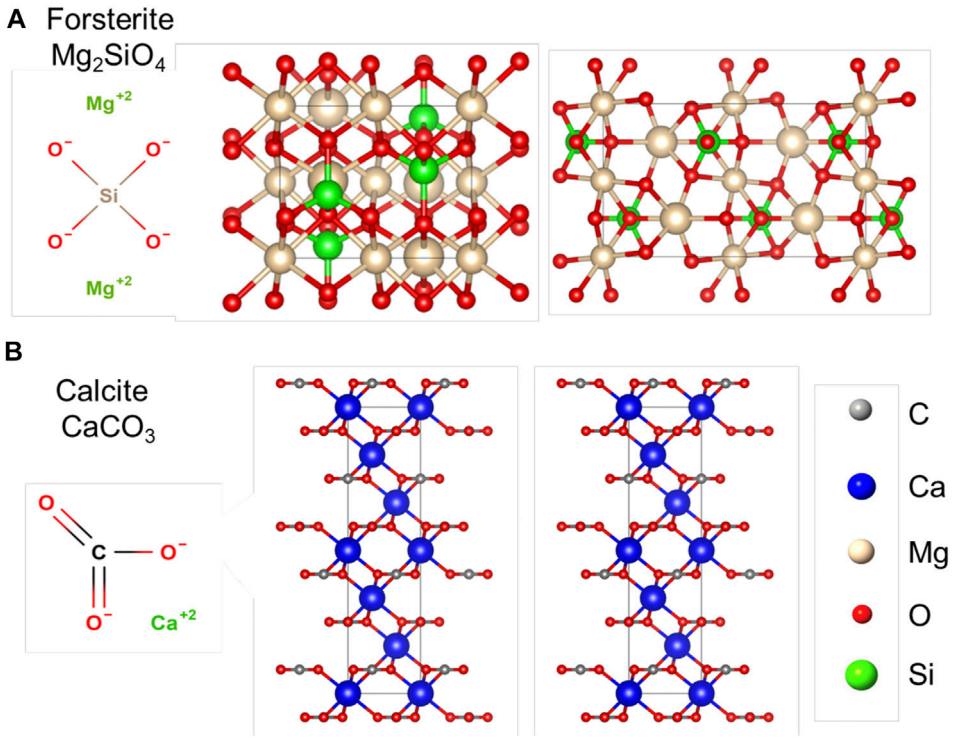

FIGURE 9
Crystal molecular structure. **(A)** Forsterite Mg_2SiO_4. **(B)** Calcite $CaCO_3$. The visualization prepared with the open source software VESTA.

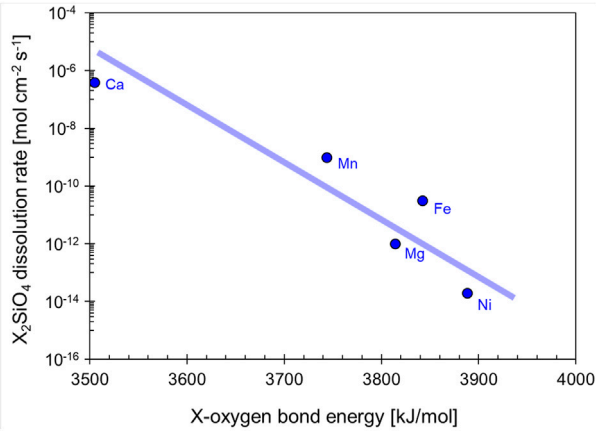

FIGURE 10
Olivine dissolution rate as a function of the metal-oxygen bond energy. X represents one of the metallic ions commonly found in olivine, such as: Ca^{2+}, Mn^{2+}, Fe^{2+}, Mg^{2+}, Ni^{2+}. Data sources: Huggins and Sun., 1946, Casey., 1991.

Chemical bonds in minerals

Oxygen and metals Ca, Mg, Fe, Mn, Ni become oppositely charged by electron transfer and form ionic bonds, whereas silicon Si, carbon C, sulfur S and oxygen O bond together by sharing electron pairs in covalent bonds. Covalent bonds have higher bond energy than ionic bonds, for example, the bond energy in the covalent bond formed by silicon-oxygen is ~13,100 kJ/mol, and the bond energy in the ionic bond formed by magnesium-oxygen is ~3,816 kJ/mol (Huggins and Sun., 1946). Therefore, metal-oxygen bond breakage prevails in mineral dissolution and controls the dissolution rate (Figure 10). In addition, amorphous minerals dissolve more readily than their crystalline counterparts, such as basaltic glass compared with crystalline basalt.

Mineral dissolution

In the presence of water, a mineral liberates ions (reactants) that move away from the mineral surface to the bulk solution mainly due to electrical interaction within the Helmholtz layer and random vibration. Ions experience the greatest potential change across the Helmholtz layer, and eventually form activated complexes and new reaction products in the bulk solution (Hayes and Katz., 1996; Crundwell., 2014). Common mineral and glass dissolution reactions in CO_2 acidified water are summarized in Table 1 (see also Espinoza et al., 2011; Kim and Santamarina., 2014). Figure 11 shows the dissolution of forsterite in CO_2 acidified water. Dissolution involves the breaking of magnesium-oxygen bonds and the release of Mg^{2+} and SiO_4^{4-};

TABLE 1 Common mineral dissolution reactions in CO_2 acidified water.

Mineral		Reaction
Silicates	Forsterite	$Mg_2SiO_4+4H^+\rightarrow 2Mg^{2+}+SiO_2+2H_2O$
	Olivine	$(Mg_{0.80}Fe_{0.20})_2SiO_4+4H^+\rightarrow 1.60Mg^{2+}+0.40Fe^{2+}+SiO_2+2H_2O$
		$(Mg_{0.43}Fe_{0.57})_2SiO_4+4H^+\rightarrow 0.86Mg^{2+}+1.14Fe^{2+}+SiO_2+2H_2O$
	Fayalite	$Fe_2SiO_4+4H^+\rightarrow 2Fe^{2+}+SiO_2+2H_2O$
	Enstatite	$MgSiO_3+2H^+\rightarrow Mg^{2+}+SiO_2+H_2O$
	Orthopyroxene	$Mg_{0.38}Fe_{0.62}SiO_3+2H^+\rightarrow 0.38Mg^{2+}+0.62Fe^{2+}+SiO_2+H_2O$
	Ferrosilite	$FeSiO_3+2H^+\rightarrow Fe^{2+}+SiO_2+H_2O$
	Anorthite	$CaAl_2Si_2O_8+8H^+\rightarrow Ca^{2+}+2Al^{3+}+2SiO_2+4H_2O$
	Ablite	$NaAlSi_3O_8+4H^+\rightarrow Al^{3+}+Na^+ +3SiO_2+2H_2O$
	Wollastonite	$CaSiO_3+2H^+\rightarrow Ca^{2+}+SiO_2+H_2O$
	Clinochlore	$Mg_5Al_2Si_3O_{10}(OH)_8 + 16H^+\rightarrow 5Mg^{2+}+2Al^{3+}+3SiO_2+12H_2O$
	Daphnite	$Fe_5Al_2Si_3O_{10}(OH)_8 + 16H^+\rightarrow 5Fe^{2+}+2Al^{3+}+3SiO_2+12\ H_2O$
	Epidote	$Ca_2FeAl_2Si_3O_{12}(OH)+13H^+\rightarrow 2Ca^{2+}+Fe^{2+}+2Al^{3+}+3SiO_2+7\ H_2O$
	Ferroactinolite	$Ca_2Fe_5Si8O_{22}(OH)_{\ 2} + 14H^+\rightarrow 2Ca^{2+}+5Fe^{2+}+8SiO_2+8H_2O$
	Prehnite	$Ca_2Al_2Si_3O_{10}(OH)_{\ 2} + 10H^+\rightarrow Ca^{2+}+2Al^{3+}+3SiO_2+6H_2O$
	Tremolite	$Ca_2Mg_5Si_8O_{22}(OH)_2 + 14H^+\rightarrow 2Ca^{2+}+5Mg^{2+}+8SiO_2+8H_2O$
	Wairakite	$CaAl_2Si_4O_{10}(OH)_4+8H^+\rightarrow Ca^{2+}+2Al^{3+}+4SiO_2+6H_2O$
	Forsterute	$Mg_2SiO_4+4H^+\rightarrow 2Mg^{2+}+SiO_2+2H_2O$
	Diopside	$MgCaSi_2O_6+4H^+\rightarrow Mg^{2+}+Ca^{2+}+2SiO_2+2H_2O$
Carbonates	Calcite	$CaCO_3+H^+\rightarrow Ca^{2+}+HCO_3^-$
	Magnesite	$MgCO_3+H^+\rightarrow Mg^{2+}+ HCO_3^-$
	Siderite	$FeCO_3+H^+\rightarrow Fe^{2+}+ HCO_3^-$
	Dolomite	$CaMg(CO_3)_2+2H^+\rightarrow Ca^{2+}+Mg^{2+}+2HCO_3^-$
Oxides	Hematite	$Fe_2O_3+6H^+\rightarrow 2Fe^{3+}+ 3H_2O$
	Magnetite	$Fe_3O_4+8H^+\rightarrow 2Fe^{3+}+ Fe^{2+}+ 4H_2O$
	Corundum	$Al_2O_3+6H^+\rightarrow 2Al^{3+}+ 3H_2O$
Sulfide	Pyrite	$FeS_2+H_2O\rightarrow Fe^{2+}+0.25SO_4^{2-}+0.25H^+ +1.75HS^-$
	Pyrrhotite	$FeS + H^+\rightarrow Fe^{2+}+HS^-$
Sulfate	Gypsum	$CaSO_4{\cdot}2H_2O\rightarrow Ca^{2+}+SO_4^{2-}+2H_2O$
Halide	Halite	$NaCl\rightarrow Na^+ +Cl^-$
Basalt glass (Gysi and Stefánsson, 2012)		$K_{0.008}Na_{0.08}Ca_{0.27}\ Mg_{0.26}Mn_{0.003}S_{0.002}Ti_{0.02}Fe^{2+}_{0.169}Fe^{3+}_{0.012}Al_{0.35}Si_{1.00}O_{3.327} + 1.128H^+ + 2.201H^2O = 0.008\ K^+ + 0.08Na^+ + 0.27Ca^{2+} + 0.26\ Mg^{2+} + 0.003Mn^{2+} + 0.002HS^- + 0.02Ti(OH)^4 + 0.169Fe^{2+} + 0.012Fe(OH)^{4-} + 0.35Al(OH)^{4-} + H^4SiO^4$

subsequently, Mg^{2+} ions form hydrated ions with water, while SiO_4^{4-} ions form activated complexes with protons, $HSiO_4^{3-}$.

Kinetics of mineral dissolution

The rate of dissolution far-from-equilibrium r_d [mol/s] can be estimated as (Arthur et al., 2000):

$$r_d = k \cdot s \cdot a_{H^+}^{n_{H^+}} \tag{14}$$

where k [mol m^{-2} s^{-1}] is the rate constant for mineral dissolution, s [m^2] is the surface area of minerals in a reference volume of solution, and n_{H^+}[ ] is the reaction order with respect to the activity of protons a_{H^+} [ ]. The mineral surface area varies during dissolution (Grandstaff., 1978; Gautier et al., 2001; Fischer et al., 2012).

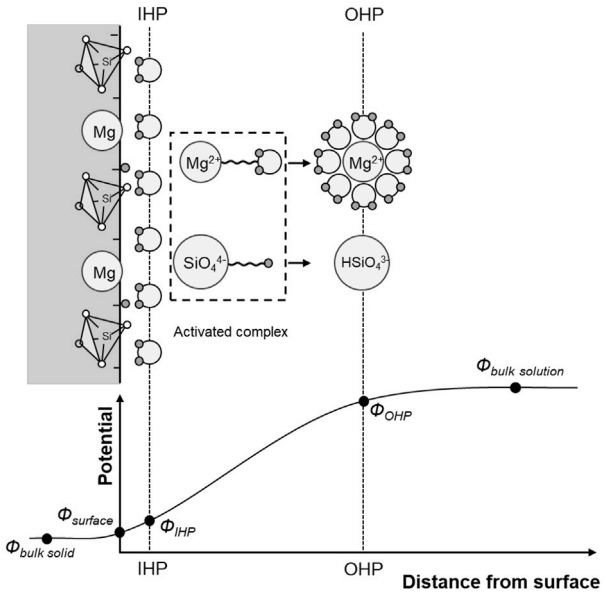

FIGURE 11
Stages in forsterite Mg_2SiO_4 dissolution—OHP: outer Helmholtz plane. IHP: inner Helmholtz plane. After Crundwell., 2014.

Table 2 lists kinetic dissolution rates calculated using Eq. 14 and kinetic parameters compiled from the literature for common silicate and carbonate minerals in acid solutions. Clearly, carbonates are more reactive than other minerals, in agreement with their bond energies reported above. Anorthite, fayalite and forsterite have higher reactivity than other silicates due to the relative abundance of ionic metal-oxygen bonds and the absence of silicon-oxygen covalent bonds in these minerals (Angel., 1988; Velbel., 1999). Other parameters affect mineral dissolution rates as well, for example: temperature, pH, CO_2 partial pressure (Stumm and Morgan., 1996), salinity (Pokrovsky et al., 2005), organic ligands (Fredd and Fogler., 1998), and catalysts (e.g., sodium bicarbonate–O'Connor et al., 2001).

Mineral dissolution: Hydro-chemo-mechanical coupling

Minerals dissolve during CO_2 injection and produce species that are carried away by advection and diffusion. Consequently, mineral dissolution enhances porosity and permeability, and causes settlement and stress changes.

The evolution of mineral dissolution in a porous medium is inherently related to pore size variability and the presence of preferential flow pathways which deliver the majority of the reactants in advective regimes: 10% of pores may be responsible for more than 50% of the total flow rate in sediments (Jang et al., 2011), and flow channeling is even more pronounced in fractured rock masses (National Academies of Sciences Engineering and Medicine, 2020; Cardona et al., 2021). Therefore, dissolution and transport are coupled, and may involve fabric changes. Hydro-chemo-mechanical coupling effects triggered by dissolution are explored next.

Dissolution at constant fabric (no mechanical coupling)

Dissolution and advection lead to increased flow focusing and "wormhole" formation (Kim and Santamarina., 2015; Kim and Santamarina., 2016; Menke et al., 2017; Derr et al., 2020). Two dimensionless ratios combine the three time scales for advection t_{adv}, diffusion t_{diff}, and reaction t_r; for a channel length L_{ch},

$$\text{Damköhler number} \quad \text{Da} = \frac{t_{adv}}{t_r} = \frac{kL_{ch}}{v} \tag{15}$$

$$\text{Péclet number} \quad \text{Pe} = \frac{t_{diff}}{t_{adv}} = \frac{vL_{ch}}{D} \tag{16}$$

where v [m/s] is the average flow velocity in pores, D [m^2/s] is the molecular diffusion coefficient, and the kinetic rate κ [1/s] = kS_sM_m is a function of the rate constant for mineral dissolution k [mol m^{-2} s^{-1}], the mineral specific surface area S_s [m^2/g], and the mineral molar mass M_m [g/mol]. Various dissolution topologies become apparent in the Péclet-Damköhler *Pe-Da* diagram in Figure 12: compact dissolution, conical wormhole, dominant wormhole, ramified wormhole and uniform dissolution regimes. Low advection velocities, i.e., long t_{adv} and small *Pe*, allow reactant consumption near the inlet and instabilities cannot develop; conversely, very high advection velocities, i.e., short t_{adv}, high *Pe* and small *Da*, carry reactants all along the porous medium from inlet to outlet and favor a stable homogeneous dissolution. Wormholes develop at intermediate flow rates, i.e., large *Da* and *Pe*, so that reactants act preferentially along flow channels.

Similarly, various dissolution regimes emerge when reactive fluids flow through rock fractures (Kim and Santamarina., 2015; Shafabakhsh et al., 2021). A low *Da* causes a more uniform aperture enlargement along the length of the fracture. On the other hand, most reactants are consumed near the inlet in large *Da* and low *Pe* regimes (highly reactive low-advection conditions). Finally, a large fracture aperture slows the diffusive transport of reactants to the mineral fracture surface, and higher reactant concentrations remain along the centerline.

Dissolution-triggered fabric changes (mechanically coupled effects)

Mineral dissolution during CO_2 injection can cause fabric changes in sediments, block sliding in fractured rocks and stress changes in both cases.

The coefficient of lateral earth pressure at rest $k_0 = \sigma_h'/\sigma_v'|_{\varepsilon h=0}$ is the stress ratio between the effective horizontal stress σ_h' and the effective vertical stress σ_v' under zero lateral strain conditions $\varepsilon_h = 0$. Both experimental and numerical results show that even a

TABLE 2 Kinetic rate parameters for mineral dissolution in acid solutions (T = 25°C) and the calculated dissolution rates r (Eq. 14—Calculations assume 25°C, 0.1 MPa, the pH of CO_2 water is 4.5, the surface area is fixed at 2 m^2).

Minerals		Log k (mol m^{-2} s^{-1})	n	pH	References	r (mol s^{-1})
Silicates	Mg_2SiO_4 (Forsterite)	-6.85	0.470	0	Palandri and Kharaka., 2004	1.09×10^{-4}
	Fe_2SiO_4 (Fayalite)	-4.8	1.0	acid	Sverdrup., 1990	1.00×10^{1}
	$MgSiO_3$ (Enstatite)	-9.3 ± 0.7	-0.25 ± 0.14	2–7	Furrer et al., 1993	4.23×10^{-11}
	$Mg_{0.38}Fe_{0.62}SiO_3$ (Orthopyroxene)	-9.8 ± 0.3	-0.49 ± 0.13	<5	Schott and Berner., 1983	6.40×10^{-13}
	$FeSiO_3$ (Ferrosilite)	-9.3 ± 0.3	-0.33 ± 0.06	2.1-7.1	Banfield et al., 1995	1.53×10^{-11}
	$CaAl_2Si_2O_8$ (Anorthite)	-5.87	1.12	≤5	Brady and Walther., 1989	3.90×10^{0}
	$NaAlSi_3O_8$ (Albite)	-9.5	0.5	acid	Sverdrup., 1990	7.96×10^{-9}
	$CaSiO_3$ (Wollastonite)	-8.0 ± 0.2	-0.24 ± 0.04	≤7.2	Xie., 1994	9.57×10^{-10}
	$Ca_2FeAl_2Si_3O_{12}(OH)$ (Epidote)	-10.60	0.338	0	Palandri and Kharaka., 2004	3.63×10^{-9}
	$Ca_2Fe_5Si8O_{22}(OH)_2$ (Ferroactinolite)	-8.9 ± 0.2	-0.75 ± 0.06	3.6–4	Zhang., 1990	1.89×10^{-13}
	$Ca_2Al_2Si_3O_{10}(OH)_2$ (Prehnite)	-10.66	0.256	0	Palandri and Kharaka., 2004	1.12×10^{-9}
	$Ca_2Mg_5Si_8O_{22}(OH)_2$ (Tremolite)	-11.5	0.11	1–6	Schott et al., 1981	2.55×10^{-11}
	Mg_2SiO_4 (Forsterute)	-10.85	-0.47	0	Palandri and Kharaka., 2004	7.35×10^{-14}
	$MgCaSi_2O_6$ (Diopside)	-9.4 ± 0.4	-0.22 ± 0.1	2–6	Knauss et al., 1993	4.91×10^{-11}
Carbonates	$CaCO_3$ (Calcite)	-0.30	1.000	0	Palandri and Kharaka., 2004	3.17×10^{5}
	$MgCO_3$ (Magnesite)	-6.38	0.589	0	Palandri and Kharaka., 2004	1.45×10^{-3}
	$FeCO_3$ (Siderite)	-3.19	0.500	0	Palandri and Kharaka., 2004	7.26×10^{-1}
	$CaMg(CO_3)_2$ (Dolomite)	-3.76	0.500	0	Palandri and Kharaka., 2004	1.95×10^{-1}
Oxides	Fe_2O_3 (Hematite)	-9.39	1.000	0	Palandri and Kharaka., 2004	2.58×10^{-4}
	Fe_3O_4 (Magnetite)	-8.59	0.279	0	Palandri and Kharaka., 2004	1.76×10^{-7}
Sulfide	FeS_2 (Pyrite)	-7.52	-0.500	0	Palandri and Kharaka., 2004	1.07×10^{-10}
	FeS (Pyrrhotite)	-8.04	-0.597	0	Palandri and Kharaka., 2004	9.50×10^{-12}

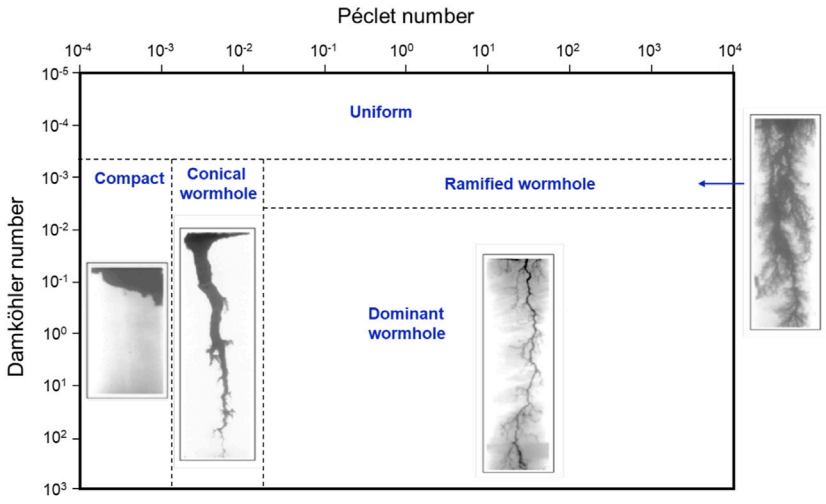

FIGURE 12
Dissolution in *rigid porous network*—Various regimes in the Péclet-Damköhler space. Modified from Golfier et al., 2002. Source of images: Fredd., 2000.

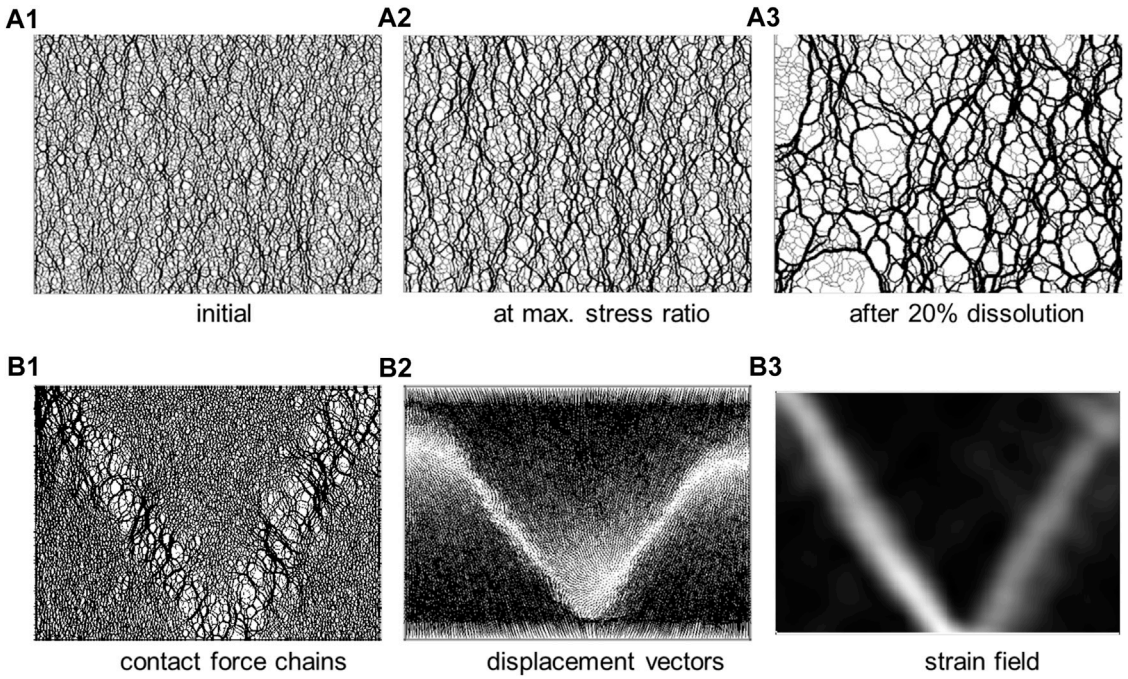

FIGURE 13
Dissolution in *granular materials* under constant vertical stress and zero lateral strain. **(A)** Force chain evolution during the dissolution of randomly distributed soluble grains: the evolving brittle "honeycomb" structure exhibits pronounced force chain arching (20% of the grains are soluble—Shin et al., 2008). **(B)** Pressure-solution whereby the particle dissolution rate is proportional to the normal force: the emergence of shear bands, Cha and Santamarina., 2019.

small amount of particle dissolution can produce a pronounced drop in k_0 and the state of stress may even reach the Coulomb failure envelope, i.e., Rankine active coefficient $k_0 \rightarrow k_a$ (mixture of soluble and insoluble grains–Shin and Santamarina., 2009). At the grain scale, forces initially carried by dissolving particles get transferred to less soluble neighboring grains, the particle coordination number decreases, and force chains form a brittle honeycomb-like fabric (Figure 13A—Shin et al., 2008; Cha and Santamarina, 2014; Kim et al., 2019). After reaching its lowest value, the stress ratio may gradually recover upon further dissolution to reach a "terminal state".

Stress concentration at grain contacts favors localized dissolution, i.e., "pressure solution" (even in single-mineral systems—Rutter, 1983; Etheridge et al., 1984; Fowler and Yang., 1999). Strong intergranular force chains and force-dependent contact dissolution combine to create a positive feedback mechanism that can lead to shear localization (Cha and Santamarina, 2016—Figure 13B). This sequence of events explains the nontectonic origin of shear discontinuities and polygonal fault systems observed in marine sediments and lacustrine deposits (Cartwright et al., 2003; Shin et al., 2008; Shin et al., 2010).

Let's assume a carbonate reservoir (mineralogy = 100% calcite, porosity = 0.3) at a depth of 800 m (p = 8 MPa, T = 60 °C) filled with CO_2 saturated water (pH ≈ 3.21, calcite solubility ≈ 4.41×10^{-5} mol/L). Under these conditions, 1.3 g ~ 0.5 cm^3 of calcite will dissolve for every pore volume of CO_2 saturated water, and cause a volumetric strain of $\varepsilon = 0.5 \times 10^{-6}$. The induced isotropic stress change is $\Delta\sigma = E \times \varepsilon \approx 1$ kPa per

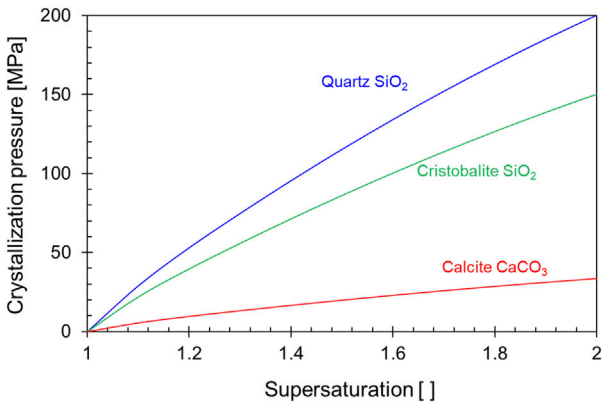

FIGURE 14
Crystallization pressures of quartz, cristobalite, and calcite as a function of supersaturation Trends from Wiltschko and Morse., 2001; formulation in Maliva and Siever., 1988.

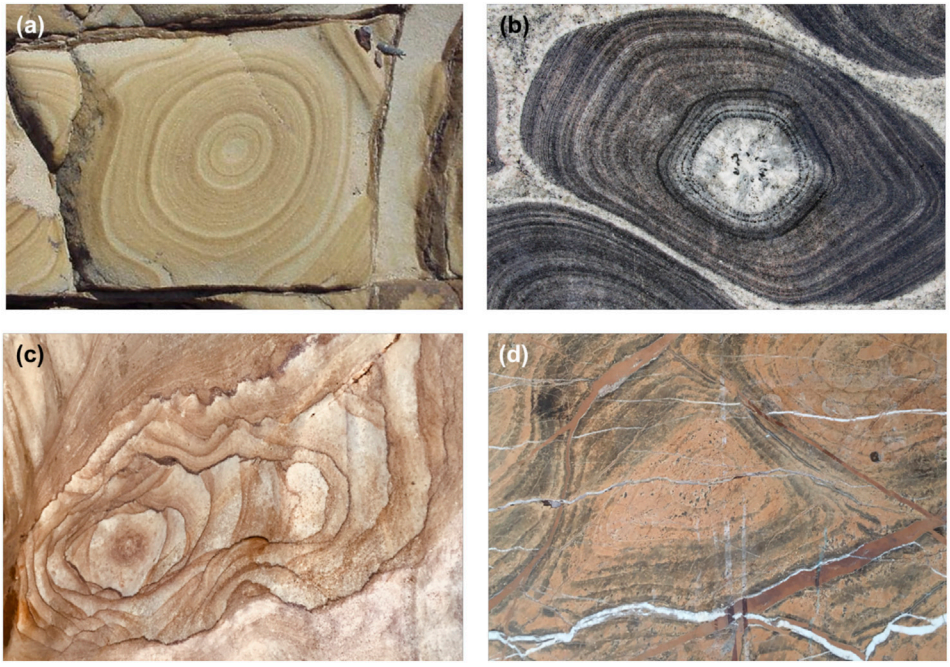

FIGURE 15
Diffusive-reactive transport: Liesegang bands. **(A)** in sandstone - from T McCarron. **(B)** Orbicular granite—Lahti et al., 2005. **(C)** Sandstone—Wadi Lajab, Saudi Arabia. **(D)** Jordanian carbonate.

pore volume of fluid exchange (the Young's modulus is $E \approx 5$ GPa for a carbonate with porosity 0.3—Ng and Santamarina 2022). Thus, the stress change for a single pore volume is small; however, ensuing convective transport and dissolution localization may eventually trigger mechanical instabilities.

Precipitation: Crystallization pressure and matrix filling

Precipitation is a self-homogenizing process in porous media: precipitates reduce the permeability of preferential flow paths and reactive fluids deviate to other pathways. Still, precipitation has other important consequences related to crystallization pressure and ensuing pore habits. These processes play a central role in CO_2 mineralization.

Crystallization pressure: new fractures

New minerals nucleate on preexisting surfaces (heterogeneous nucleation), grow into the pore space, and exert crystallization pressure when growth is constrained by pore and fracture walls (Lee and Kurtis, 2017). A thin film between the crystal and the wall and corner flow (along roughness and crevices which are not occupied by the growing mineral) maintain connectivity with the saturated solution and sustain crystal growth (Becker and Day, 1916; Taber, 1916; Correns, 1949).

The crystal experiences an internal excess pressure $\Delta P = P_{crys} - P_{sol}$, where P_{crys} is the pressure in the growing crystal and P_{sol} is the hydrostatic pressure of the pore solution. This excess pressure ΔP is a function of the solution supersaturation $S = c/c_0$, where c and c_0 are the solute concentrations in the supersaturated solution and in the saturated solution respectively:

$$\Delta P = P_{crys} - P_{sol} = \frac{RT}{V_m} lnS \tag{17}$$

Other parameters include: the gas constant R [J mol^{-1} K^{-1}], the absolute temperature T [K], and the molar volume of the precipitated solid phase V_m [m^3/mol]. Figure 14 shows the calculated crystallization pressure of quartz SiO_2, cristobalite SiO_2 and calcite $CaCO_3$ for different degrees of supersaturation (Wiltschko and Morse, 2001).

The stress field induced by the crystallization pressure in neighboring pores may trigger an opening mode fracture (Anderson, 2017). Similarly, precipitation may form grain-displacive nodules and lenses in sediments when the crystallization pressure exceeds the *in situ* effective stress (Shin and Santamarina, 2011; Liu and Santamarina, 2022). Note that precipitated carbonates usually occupy a larger volume than the dissolved source minerals (Snæbjörnsdóttir et al., 2018; Snæbjörnsdóttir et al., 2020), therefore volume

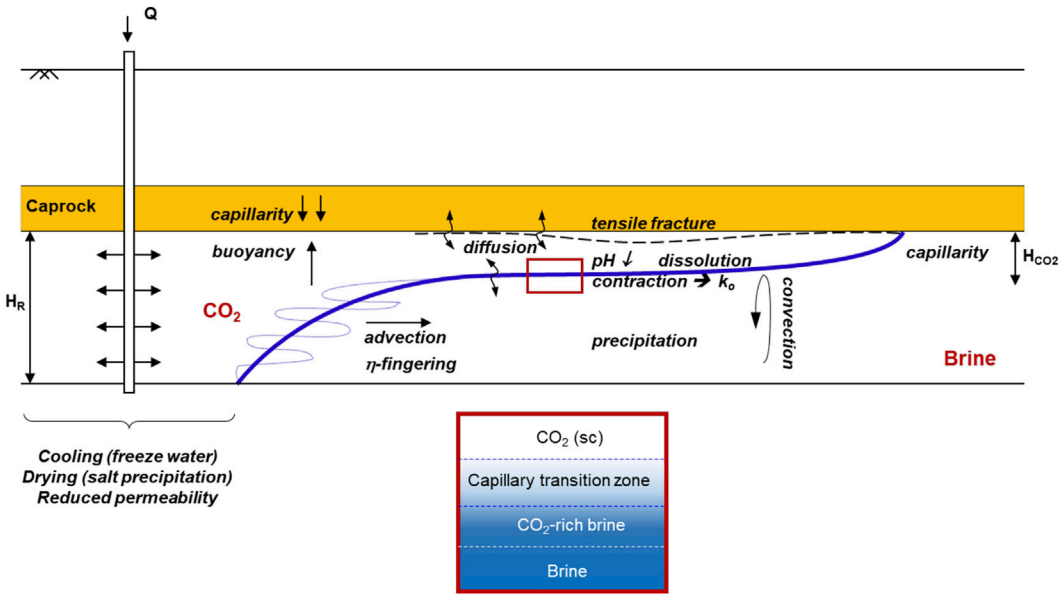

FIGURE 16
Carbon geological storage in saline aquifer: reservoir zones and underlying phenomena near the injection well and in the far field.

expansion during local dissolution-precipitation will also cause crystallization pressure.

Recurrent precipitation in the matrix: Liesegang band formation

Crystal growth decreases the local reactant concentration and may locally deplete the reactants that the host medium may contribute. Meanwhile, the reaction front keeps advancing; eventually transported and host rock reactants reach the threshold saturation concentration again and a new round of mineral precipitation starts. Such reactive-diffusion-precipitation process produces a periodic precipitation pattern, known as Liesegang bands (Liesegang, 1896; Rácz, 1999; Panjarian and Sultan, 2001; Nabika et al., 2020). Banded precipitation is found in a wide range of geological settings; Figure 15 shows periodic precipitation patterns in sandstones, carbonate and granite. These field observations are natural analogues for CO_2 mineralization within the rock matrix.

CO2 mineralization

The general reaction for CO_2 mineralization starts with calcium, magnesium or iron silicates to produce the corresponding carbonates:

$$(Ca, Mg, Fe)SiO_3 + CO_2 + H_2O \rightarrow (Ca, Mg, Fe)CO_3 + H_2SiO_3 \quad (18)$$

Mafic and ultramafic rocks are silicates; therefore, the ultimate storage ability per cobic meter of rock is determined by the molar mass ratio between CO_2 and silicate M_{CO2}/M_{silic}, and the rock density and porosity $(M_{CO2}/M_{silic})\cdot(1\text{-}\phi)\rho_{rock}$. The molar mass ratios M_{CO2}/M_{silic} are: 0.38 for wollastonite $CaSiO_3$, 0.44 for enstatite $MgSiO_3$ and 0.33 $FeSiO_3$ for ferrosilite. Then, the theoretical ultimate storage density values can exceed 500 kg/m^3. However, the reaction is time-dependent and more modest values between 30-and-200 kg CO_2 per cubic meter of basalt could be expected within the first 10-to-100 years after injection (e.g., Xiong et al., 2018).

In fact, the reaction rate depends on the mineral reactivity, the available exposed surface area and fracture spacing, and the evolving efficiency of transport processes. Eq. 14 and kinetic parameters in Table 2 show that the characteristic time for carbonation varies in orders of magnitude for different minerals. For example, consider a rock block with a constant exposed surface of 2 m^2 in contact with CO_2 saturated water (p = 0.1 MPa, T = 25°C, pH = 4.5): it takes around 7 years to dissolve 1 m^3 forsterite Mg_2SiO_4 (ρ = 3,270 kg/m^3) but 40,000 years for albite $NaAlSi_3O_8$ (ρ = 2,620 kg/m^3). These times are for reaction-limited processes; advection or diffusion-limited transport may eventually determine the rate of mineralization under reservoir conditions.

Other phenomena—reservoirs

The geological storage of CO_2 involves other reservoir-dependent processes, such as zone differentiation and convective currents in saline aquifers, excess pressure due to

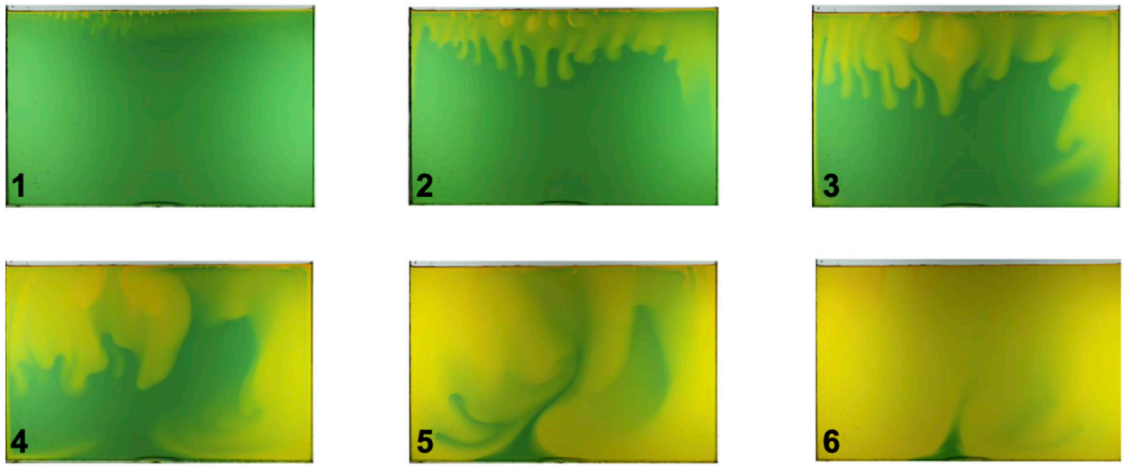

FIGURE 17
CO_2 solute driven convection. Time lapse images of a water bath beneath a CO_2 atmosphere (water with a universal pH indicator—Bang et al., 2012). The time interval between images is 40 min.

the buoyant CO_2 plume and altered seal performance, oil mobilization in depleted reservoirs, and near-well drying and cooling. These phenomena are investigated next.

CO_2 injection into saline aquifers

Transport during CO_2 injection into saline aquifers involves advection, dispersion, dissolution, diffusion, and convection (Figure 16). CO_2 is lighter and less viscous than water, therefore, CO_2 injection responds to buoyant, capillary and viscous forces: 1) CO_2 invasion next to the well is most sensitive to stratification and invades by viscous fingering through the most pervious layers, 2) the plume becomes gravity-dominant away from the well (Hesse et al., 2008), and eventually 3) it rests against the top seal by buoyancy and capillary trapping. Then, the reservoir develops various zones according to the saturating fluids: the supercritical CO_2 plume, the capillary transition zone, CO_2-rich brine, and the far-field saturated with the initial brine (Figure 16).

During early storage times, the degree of water saturation in the reservoir is a function of the capillary pressure $P_c = (\gamma_w - \gamma_{CO2})H_{CO2}$, where H_{CO2} is the height of the CO_2 column, as predicted by the reservoir capillarity-saturation response $S_w = f(\Delta u)$ often captured with Brooks-Corey or van Genuchten models. The degree of water saturation decreases with time as water dissolves in CO_2 and is transported away by diffusion.

Next to the plume lower boundary, stored CO_2 dissolves into the groundwater and convection emerges due to the increased density of water with dissolved CO_2 - between $\Delta\rho/\rho_O$ = 0.1 and 1% depending on pressure and temperature (Emami-Meybodi et al., 2015. Note: water acidified with carbonic acid dissolves minerals and experiences an even larger increases in density–see previous sections). The Rayleigh number Ra compares the rate of fluid convection with the rate of diffusive transport:

$$\mathrm{Ra} = \frac{k_{hy} g H_R \Delta\rho\rho_0}{\mu_w D} \tag{19}$$

where the governing parameters are the formation permeability k_{hy} [m^2], g = 9.8 m/s^2, the height of the fluid column H_R [m], the change in fluid density $\Delta\rho$ [kg/m^3], the viscosity of water μ_w [Pa·s], and the diffusion coefficient of CO_2 in water D [m^2/s]. Convection typically occurs when $Ra > 4\pi^2$ (Kneafsey and Pruess, 2010). Figure 17 shows time-lapse images of emerging convective currents when CO_2 gas rests above an aquifer at atmospheric pressure; the pH indicator changes in color from green to yellow at pH = 5. Small fingers initiate at the interface and begin to grow. Then there is an increase in the finger wavelength and a decrease in the number of fingers.

The convection period is $t_{cov} = \frac{\mu H_R}{k_{hyd} g \Delta\rho}$ (Jiang et al., 2019) then, for an aquifer of thickness H_R = 10 m and permeability k_{hyd} = 20 md, the convection period is t_{cov} = 150 years assuming $\Delta\rho$ = 10 kg/m^3.

Finally, the injection of dry CO_2 into a saline aquifer causes salt precipitation as water evaporates into the supercritical CO_2 near the wellbore (Miri et al., 2015). Salt precipitation can reduce CO_2 injectivity into the reservoir; its impact depends on the injection rate, mode (monotonic vs. cyclic), and brine salinity (Talman et al., 2020; He et al., 2022).

Seal rock: structure trapping

Small pores in high specific surface clay-rich caprocks give rise to the high capillary entry pressure and low permeability needed to hinder the upwards migration of the buoyant CO_2 plume. On the other hand, CO_2 invasion either dissolved in water or as a supercritical phase alters the physiochemical equilibrium in the seal rock.

Capillary pressure against the seal

The plume height h [m] determines the excess pressure in the CO_2 plume at the seal-reservoir interface, $\Delta P = P_{CO2} - P_w = (\rho_w - \rho_{co2})gh$. On the other hand, the capillary breakthrough pressure P_c the seal may resist is a function of the interfacial tension γ [N/m] between water and CO_2 at reservoir pressure and temperature conditions, the contact angle θ formed by the water-CO_2 interface on the mineral surface, and the characteristic pore diameter d^* [m] for the percolating path across the seal layer.

$$P_c = \frac{\gamma \cos\theta}{d^*} \tag{20}$$

The characteristic pore diameter d^* is a function of the specific surface area S_s, the void ratio e, the mineral density ρ_m, a fabric factor ψ and a β factor related to the pore size distribution along percolating paths: $d^* = \beta\psi e/(Ss.\rho_m)$ (Espinoza and Santamarina, 2010; Espinoza and Santamarina, 2017). Then, the sealing number Π_{seal} compares the capillary breakthrough pressure P_c to the buoyant pressure ΔP:

$$\Pi_{seal} = \frac{P_c}{\Delta P} = \frac{\gamma \cos\theta S_s \rho_m}{\beta\psi e\left(\rho_w - \rho_{CO_2}\right) gh} \tag{21}$$

Sealing numbers $\Pi_{seal} \gg 1$ are expected for safe storage. Clearly, a high sealing number is found for small plume thickness h, and high specific surface Ss clayey seals.

On the other hand, the higher CO_2 pressure changes the effective stress can trigger fault reactivation and grain-displacive breakthrough. The stability number $\Pi_{stability}$ compares the initial horizontal effective stress σ'_{h0} at the reservoir depth z to the capillary pressure ΔP created by a CO_2 plume of thickness h.

$$\Pi_{stability} = \frac{\sigma'_{h0}}{\Delta P} = \frac{(\sigma_{z0} - P_0)k_0}{hg\left(\rho_w - \rho_{CO_2}\right)} \tag{22}$$

where the variables are: the initial total vertical stress σ_{z0} and fluid pressure P_0 at the reservoir-seal interface before CO_2 injection, and effective stress ratio $k_0 = \sigma_h'/\sigma_z'$ at zero lateral strain. Safe CO_2 injection requires reservoirs with a high stability number $\Pi_{stability}$. The organic matter in a shale is CO_2-wet (Arif et al., 2017b), therefore, low organic content shales are preferred for CO_2 seal.

CO2 interaction with clay-rich caprock

As anticipated by the sealing number Π_{seal}, clayey shales are promising seal layers for CO_2 geological storage. Hence, we must address the hydro-chemo-mechanical coupling between CO_2 and clay minerals. We can anticipate two salient effects:

1) *First contact (before SC-CO_2 invasion)*: CO_2 dissolves in water and acidifies the brine. Low pH promotes protonation, and leads to positively charged surfaces, which will affect the clay fabric.
2) *Long term (after SC-CO_2 invasion)*: CO_2 replaces water and becomes the saturating pore fluid. There will be a reduction in osmotic repulsion, dissolution of residual water in CO_2 and salt precipitation, volumetric contraction driven by capillarity, and a three-fold increase in the Hamaker constant for clay-CO_2-clay as compared to clay-water-clay (Shin and Santamarina, 2010; Espinoza and Santamarina, 2012).

Changes in electrical and capillary forces will induce volumetric changes, thus stress changes in the caprock. Figure 18 shows that a montmorillonite-water paste contracts and experiences desiccation cracks when water evaporates into supercritical CO_2 atmosphere. Sedimentation experiments show that clay particles show strong particle aggregation with heptane and liquid CO_2 which shows that the electrical interaction between clays and water is different than with CO_2 in its different states (Espinoza and Santamarina, 2012).

CO_2 injection into depleted oil reservoirs

CO_2 injection into depleted oil reservoirs benefits from time-proven seals. In addition, CO_2 can mobilize residual oil; in this case, we can simultaneously sequester CO_2 while recovering additional oil. Numerous pore-scale mechanisms affect CO_2-oil displacement processes, including oil swelling, ganglia destabilization, coalescence of disconnected oil blobs into a continuous oil phase, light-component extraction, miscible displacement and asphaltene deposition. Details follow.

Oil density and viscosity

The oil density decreases slightly with temperature, and pressure has a second order effect (Figure 1). On the other hand, the viscosity of crude oils can decrease by an order of magnitude when the temperature increases from 40°C to 80°C (Figure 3).

Oil-water interfacial tension

The interfacial tension between two non-polar fluids such as CO_2 and oil tends to be smaller than when dipolar water molecules are involved. Figure 19 shows the interfacial tension

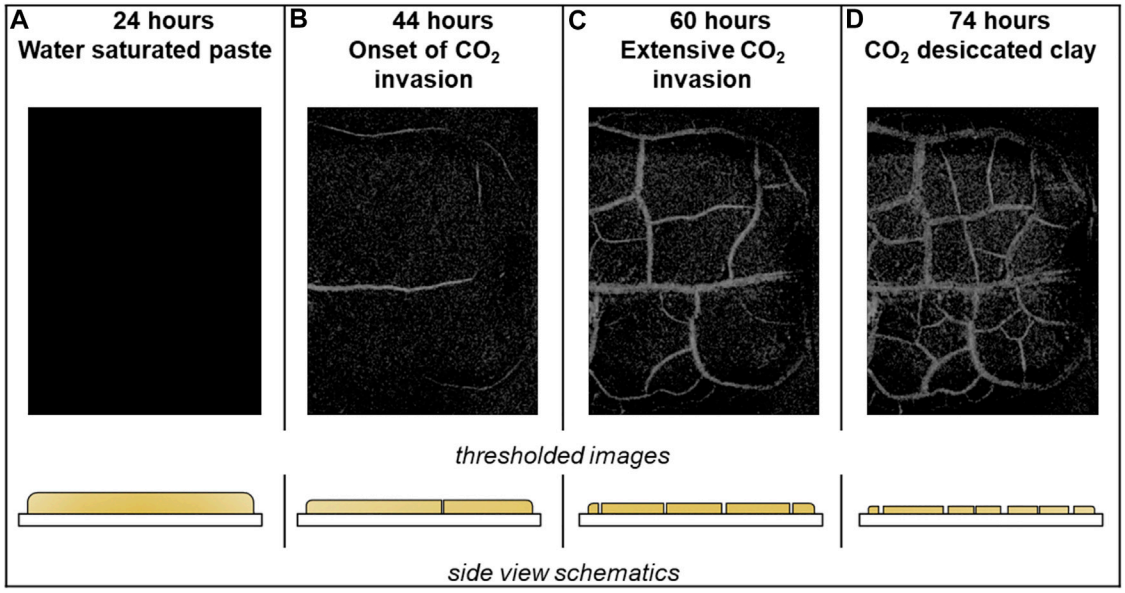

FIGURE 18
Montmorillonite-water paste subjected to a supercritical CO_2 atmosphere (p = 15 MPa and T = 38°C). The photographs and associated sketches show the evolution of desiccation and the formation of capillary-driven fractures: as water evaporates into the CO_2 reservoir, suction increases and the water-CO_2 interface "compresses" the sediment; eventually, supercritical CO_2 invades the sediment and triggers desiccation cracks, Espinoza and Santamarina., 2012.

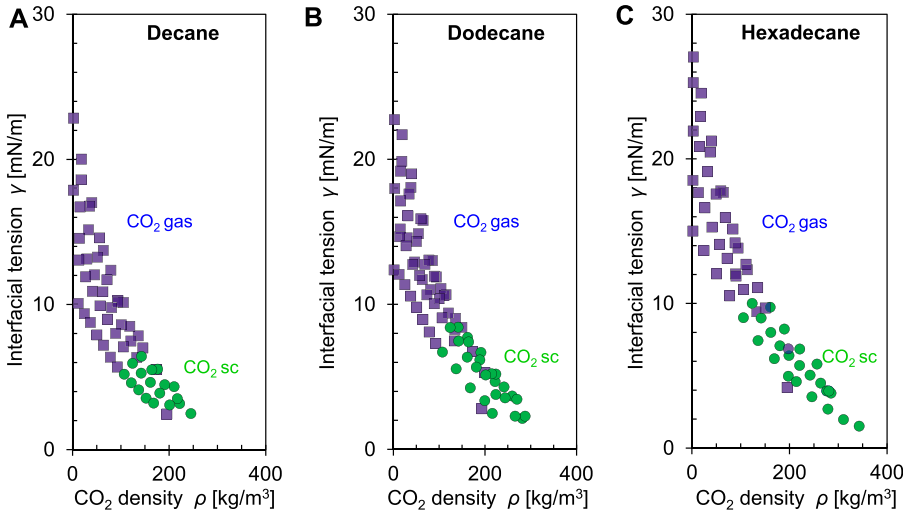

FIGURE 19
Interfacial tension between selected alkanes and CO_2 as a function of the CO_2 density at different pressures and temperatures: **(A)** Decane, **(B)** Dodecane and **(C)** Hexadecane. Symbols: CO_2 gas (■) and CO_2 supercritical (●). Data source: Georgiadis et al., 2010.

between three different alkanes (decane, dodecane and hexadecane) and CO_2 as a function of CO_2 density. The interfacial tension increases with the number of carbon atoms in alkanes and decreases with increasing CO_2 density.

CO2 solubility in crude oil - Viscosity

The solubility of CO_2 in crude oil is much higher than in water because of their shared non-polar nature (Schmid, 2001). Solubility is directly dependent on the CO_2 partial pressure

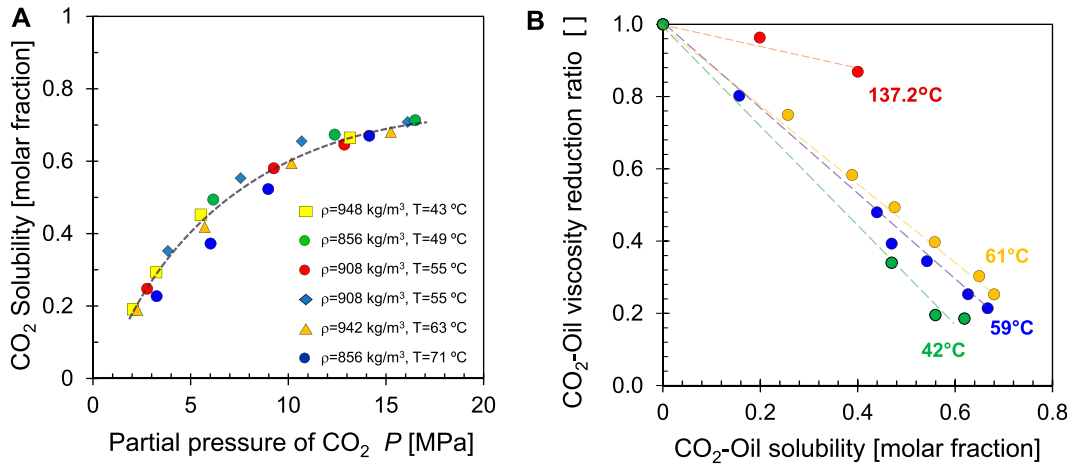

FIGURE 20
CO_2 and oil. **(A)** Solubility as a function of CO_2 partial pressure for different temperatures. Data source: Simon and Graue., 1965. **(B)** Oil viscosity with increasing molar fraction of dissolved CO_2. Data source: Barclay and Mishra., 2016.

TABLE 3 Minimum miscibility pressure for different crude oils and organic compounds.

Oil	API	Minimum miscibility pressure [MPa]	Temperature [°C]	Method	References
Light density crude oil	41	7.3	27	Vanishing interfacial tension (VIT)	Wang et al., (2010)
Light density crude oil	38	10.6	53	VIT	Gu et al., 2013
Medium density crude oil	29.5	11.7	59	Rising bubble apparatus (RBA)	Dong et al., 2013
Medium density crude oil	25.5	7.25	27	VIT	Nobakht et al., 2008
Heavy density crude oil	10	11.17	44	VIT	Li et al., 2012
Heavy density crude oil	20.2	13.09	60	VIT	Hemmati-Sarapardeh et al., 2014
Heptane	76.7	10	80	VIT	Zolghadr et al., 2013
Hexadecane	52.3	14.2	80	VIT	Zolghadr et al., 2013
Diesel	38.5	13.8	80	VIT	Zolghadr et al., 2013

(Figure 20A), and is also affected by temperature and oil properties. Oil experiences a pronounced decrease in viscosity as CO_2 dissolves in it (Figure 20B).

Crude oil and CO_2 become fully miscible and the interface vanishes when the "minimum miscibility pressure" is reached; Table 3 lists minimum miscibility pressures for various crude oils. Above the minimum miscibility pressure, a transition zone forms in the reservoir. Miscibility is not instantaneous but develops gradually, i.e., "dynamic miscibility" (Verma, 2015).

Swelling and shrinkage

Miscibility results from (1) the dissolution of CO_2 into the reservoir oil causing *swelling*, and (2) the vaporization of intermediate-molecular-weight hydrocarbons into the injected CO_2 resulting in *oil shrinkage*. The competitive effects of swelling and shrinkage are evident in the data presented in Figure 21: the oil swelling factor increases with CO_2 pressure until it reaches a maximum volume (at $p = 8$ MPa when $T = 50^{\circ}C$, or at $p = 17$ MPa when $T = 95^{\circ}C$); thereafter, vaporization-extraction becomes dominant at high-pressure and oil shrinks.

Asphaltene precipitation

Crude oil contains saturated hydrocarbons (single bonds between carbon atoms and saturated with hydrogen), aromatics (planar rings), resins, and asphaltenes. Asphaltenes are polar, polyaromatic and of high molecular weight substances that are insoluble in n-hexane or n-pentane. The size of asphaltenes ranges from less than 1 nm single molecules in light oils to more than 5 nm

aggregates in black oils and heavy oils (Mullins, 2010). CO_2 dissolution in oil causes asphaltene precipitation; as asphaltene deposits on mineral surfaces, it changes the wettability of the reservoir causing mostly irreversible formation damage. Experimental studies show that ionic liquids prevent asphaltene precipitation (Hu and Guo, 2005; Zheng et al., 2019).

Thermal effects

The injection of CO_2 triggers thermal changes in surface facilities, the injection well and inside the reservoir (Hoteit et al., 2019).

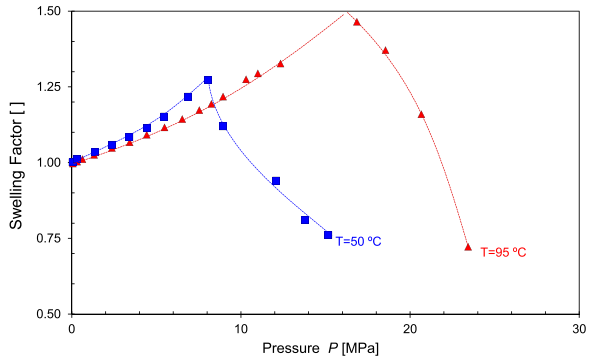

FIGURE 21
Miscibility and oil volume change. There are two competing processes: CO_2 dissolution in oil prevails at low pressure and causes oil swelling; on the other hand, light hydrocarbons vaporize into CO_2 and oil shrinks at high pressure. Data source: Rezk and Foroozesh (2019).

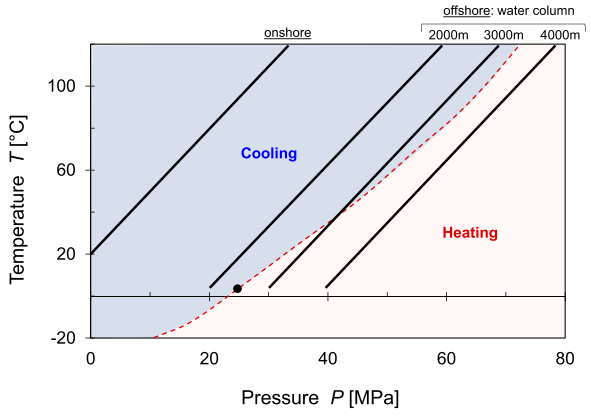

FIGURE 22
Joule-Thompson effect—Near well thermal effects. Cooling is anticipated for most onshore and offshore applications. The "inversion curve" predicts heating for seafloor injections beneath > 2,400 m high water columns.

Joule-Thomson expansion

The CO_2 injection pressure exceeds the formation pressure and rapid quasi-adiabatic expansion of CO_2 takes place near the injection well. When a gas expands from high pressure to low pressure, the temperature change ΔT is related to the pressure change ΔP by the Joule-Thomson coefficient μ_{JT} [K/Pa], which can be expressed in terms of the gas' molar volume V_m [m^3/mol], its molar heat capacity at constant pressure C_p [J K^{-1} mol^{-1}], and the coefficient of thermal expansion α[K^{-1}] as (Demirel., 2014):

$$\left(\frac{\Delta T}{\Delta P}\right) \approx \left(\frac{\partial T}{\partial P}\right)_H = \mu_{JT} = \frac{V_m}{C_p}(\alpha T - 1) \tag{23}$$

Gas expansion causes cooling when the Joule-Thomson coefficient $\mu_{JT} > 0$ and heating when $\mu_{JT} < 0$. In general, the Joule-Thomson coefficient decreases with increasing pressure and temperature (Han et al., 2010), and it is zero at the inversion point when $\alpha T - 1 = 0$ (Note: the coefficient of thermal expansion α is temperature dependent as well).

The Joule-Thomson coefficient is $\mu_{JT} \approx 10$°C/MPa for CO_2 at $T = 40$°C and $p = 5$ MPa, i.e., five times higher than for air (Phuoc and Massoudi, 2021). Figure 22 shows the Joule-Thomson inversion curve for CO_2; the auxiliary lines correspond to pressure-temperature profiles for a geothermal gradient of 30°C/km. Clearly, CO_2 expansion will cause cooling at most reservoir pressure and temperature conditions, except for injection in the seafloor under deep water columns and beneath permafrost layers.

Other thermal effects

In addition to the Joule-Thomson effect, endothermic water vaporization into supercritical CO_2 takes place mainly near the injection well (Vilarrasa and Rutqvist, 2017), while exothermic dissolution of supercritical CO_2 into the host brine prevails further away from the well (ΔH = -171.38 kJ/kg of CO_2, at p = 10.5 MPa and T = 50°C–Koschel et al., 2006). These two competing thermal effects continue until both brine and scCO_2 are saturated with the other phase.

Field implications

Under most field conditions, CO_2 injection will cause a significant temperature drop. The extent of cooling scales with the pressure drop and is partially compensated by heat transport in the reservoir (Oldenburg, 2007; Gauteplass et al., 2020). Cooling induces thermo-elastic stresses and triggers hydrate or ice formation when PT-conditions cross the corresponding phase boundary; hydrate and ice hinder fluid flow into the formation (Sloan, 2010). Effective stress changes caused by the injection pressure and thermos-elastic effects can reactivate fractures and improve their transmissivity due to shear dilation (Vilarrasa et al., 2017).

Finally, thermal changes affect density (Figures 1, 2), viscosity (Figure 3), interfacial properties (Figures 4, 5), and

solubility and pH (Figure 6). In the supercritical regime, thermally induced density gradients are most pronounced across the Widom line and near the critical point. The induced thermal gradients give rise to thermally driven convection (Islam et al., 2014).

Storage density—reservoir size

The storage capacity per unit volume of the reservoir or 'storage density' *SD* [kg CO_2/m^3 of rock] depends on the CO_2 phase and the reservoir porosity ϕ:

Dissolved:	$SC = M_{CO2}\chi_{CO2}$	$SD = 4 - \text{to} - 13 \text{kg/m}^3$
Fluid CO_2:	$SC = \rho_{CO2}$	$SD = 50 - \text{to} - 240 \text{kg/m}^3$
Hydrate:	$SC = 0.234\rho_{\text{hyd}}$	$SD = 25 - \text{to} - 77 \text{kg/m}^3$
Mineralized:	$SC = f\,(mineral,\ time,\ flux)$	$SD = 30 - \text{to} - 200 \text{kg/m}^3$

The listed *SD* values correspond to: porosity ϕ = 0.1-to-0.3, CO_2 solubility in fresh water at common reservoir PT conditions χ_{CO2} = 1 mol/l (reduce it to about half for brine—Figure 7), CO_2 molar mass M_{CO2} = 44 g/mol, CO_2 mass density ρ_{CO2} = 500-to-800 kg/m^3 (from supercritical to liquid—Figure 1), mass fraction of CO_2 in hydrate $CO_2{\cdot}8H_2O$ equal to 0.234, and hydrate density ρ_{hyd} = 1,100 kg/m^3, and attainable mineralization within the first 10-to-100 years after injection.

The annual worldwide CO_2 emission is ~40 Gt/yr. Let's consider storing 1 gigaton of CO_2, i.e., a "small fraction" of the total annual emissions: the required volume for CO_2 dissolved in fresh water is equivalent to a 30 m thick porous reservoir 50 km × 50 km wide, assuming high porosity ϕ = 0.3 and a storage density *SD* = 13 kg/m^3. Clearly, higher density CO_2 forms are preferred for efficient storage; still, the storage density *SD* values listed above imply that all CO_2 geological storage forms will require large reservoir volumes.

Conclusions

The injection of CO_2 into geological formations triggers numerous coupled thermo-hydro-chemo-mechanical processes.

The gas-liquid phase boundary and the Widom line within the supercritical regime divide the lighter gaseous-like regime from the denser liquid-like regime. The density of CO_2 has a first-order effect on the CO_2-water interfacial tension.

The CO_2-water interface pins strongly to mineral surfaces and results in a wide range of contact angles that vary between the advancing and the receding asymptotic values. Soon after injection, the residual water saturation reflects the reservoir capillary pressure vs. saturation response; thereafter, the degree of water saturation decreases with time as water evaporates into CO_2.

The solubility of CO_2 in water increases with pressure but decreases with temperature. In most geological settings, CO_2 solubility decreases with salt concentration particularly when small high-valence ions are involved. Similarly, the presence of competing gases affects the solubility of CO_2 in water because of competing ions and a reduction in the partial pressure of CO_2 (at constant total pressure).

Dissolved CO_2 acidifies water and prompts mineral dissolution (silicates and carbonates). Dissolution couples with preferential advective flow channels, diffusive transport and mechanical effects to cause various dissolution patterns, internal shear failure (even under zero lateral strain conditions), and strains may localize along shear bands. Next to the plume lower boundary, convective currents may emerge due to the increased density of water with dissolved CO_2 and minerals.

CO_2 mineralization homogenizes flow pathways. Crystal growth against pore and fracture walls exert crystallization pressure that can create new fracture surfaces or cause grain-displacive mineral lenses (when the crystallization pressure exceeds the rock tensile strength or the far-field confining stress). Precipitation may also take place within the rock matrix by successive dissolution-diffusion-precipitation sequences that result in periodic precipitation patterns, i.e., Liesegang bands.

Buoyant CO_2 plumes apply excess pressure against the seal caprock and interact with clay minerals through physicochemical processes. The sealing number Π_{seal} compares the seal capillary breakthrough pressure to the excess buoyant pressure in the CO2 plume. On the other hand, the stability number $\Pi_{stability}$ compares the initial effective stress to the excess buoyant pressure. Safe CO_2 storage requires large sealing and stability numbers and careful consideration of physicochemical effects.

CO_2 injection into depleted oil reservoirs benefits from proven seal performance. At the same time, it causes light-component extraction, oil swelling, ganglia destabilization, a reduction in oil viscosity, and miscible displacement. Then, we can simultaneously sequester CO_2 while recovering additional oil through CO_2 gravity-driven enhanced oil recovery.

Rapid CO_2 depressurization near the injection well causes cooling under most anticipated reservoir conditions. Cooling may trigger hydrate and ice formation, and reduce permeability. In some cases, effective stress changes associated with the injection pressure and cooling thermoelasticity can reactivate fractures.

The CO_2 storage density in terms of kg of CO_2 per cubic meter of the reservoir depends on the CO_2 phase and the reservoir porosity ϕ. First order estimates are 4-to-13 kg/m^3 for CO_2 dissolved in water, 25-to-77 kg/m^3 for CO_2 trapped in hydrate, 30-to-200 kg/m^3 for mineralized CO_2 (attainable within the first 10-to-100 years of storage), and 50-to-240 kg/m^3 for supercritical-to-liquid CO_2 (most efficient but prone to leakage). In all cases, large reservoir volumes will be required to

store a meaningful fraction of the CO_2 that will be emitted during the energy transition (Anderson, 2017; Global status CCS, 2021).

Author contributions

All authors listed have made a substantial, direct, and intellectual contribution to the work and approved it for publication.

Acknowledgments

G. Abelskamp edited the manuscript. Support for this research was provided by the KAUST Endowment.

Conflict of interest

The authors declare that the research was conducted in the absence of any commercial or financial relationships that could be construed as a potential conflict of interest.

Publisher's note

All claims expressed in this article are solely those of the authors and do not necessarily represent those of their affiliated organizations, or those of the publisher, the editors and the reviewers. Any product that may be evaluated in this article, or claim that may be made by its manufacturer, is not guaranteed or endorsed by the publisher.

References

Akhmadiyarov, A. A., Petrov, A. A., Rakipov, I. T., and Varfolomeev, M. A. (2019). Effect of pressure, temperature and gas phase composition on the rheological properties of heavy crude oil. *IOP Conf. Ser. Earth Environ. Sci.* 282, 012021. doi:10.1088/1755-1315/282/1/012021

Anderson, T. L. (2017). *Fracture mechanics*. Boca Raton. CRC Press. doi:10.1201/9781315370293

Andrew, M., Bijeljic, B., and Blunt, M. J. (2014). Pore-scale contact angle measurements at reservoir conditions using X-ray microtomography. *Adv. Water Resour.* 68, 24–31. doi:10.1016/j.advwatres.2014.02.014

Angel, R. J. (1988). High-pressure structure of anorthite. *Am. Mineral.* 73, 1114–1119.

Arif, M., Lebedev, M., Barifcani, A., and Iglauer, S. (2017a). CO2 storage in carbonates: Wettability of calcite. *Int. J. Greenh. Gas Control* 62, 113–121. doi:10.1016/j.ijggc.2017.04.014

Arif, M., Lebedev, M., Barifcani, A., and Iglauer, S. (2017b). Influence of shale-total organic content on CO2 geo-storage potential. *Geophys. Res. Lett.* 44, 8769–8775. doi:10.1002/2017GL073532

Arthur, R. C., Savage, D., Sasamoto, H., Shibata, M., and Yui, M. (2000). *Compilation of kinetic data for geochemical calculations*. Tokai, Ibaraki (Japan): Japan Nuclear Cycle Development Inst.

Bachu, S. (2003). Screening and ranking of sedimentary basins for sequestration of CO2 in geological media in response to climate change. *Environ. Geol.* 44, 277–289. doi:10.1007/s00254-003-0762-9

Banfield, J. F., Ferruzzi, G. G., Casey, W. H., and Westrich, H. R. (1995). HRTEM study comparing naturally and experimentally weathered pyroxenoids. *Geochim. Cosmochim. Acta* 59, 19–31. doi:10.1016/0016-7037(94)00372-S

Bang, E. S., Son, J. S., and Santamarina, J. C. (2012). "Subsurface CO2 leakage : Lab-scale study of salient characteristics and assessment of borehole-based detection using resistivity tomography," in Proceeding of the 4th International Conference on Geotechnical and Geophysical Site Characterization (ISC'4), Porto de Galinhas, Pernambuco – Brazil, January 2013.

Barclay, T. H., and Mishra, S. (2016). New correlations for CO2-Oil solubility and viscosity reduction for light oils. *J. Pet. Explor. Prod. Technol.* 6, 815–823. doi:10.1007/s13202-016-0233-y

Becker, G. F., and Day, A. L. (1916). Note on the linear force of growing crystals. *J. Geol.* 24, 313–333. doi:10.1086/622342

Bell, J. G., Benham, M. J., and Thomas, K. M. (2021). Adsorption of carbon dioxide, water vapor, nitrogen, and sulfur dioxide on activated carbon for capture from flue gases: Competitive adsorption and selectivity aspects. *Energy fuels.* 35, 8102–8116. doi:10.1021/acs.energyfuels.1c00339

Bikkina, P. (2011). Contact angle measurements of CO2–water–quartz/calcite systems in the perspective of carbon sequestration. *Int. J. Greenh. Gas Control* 5 (5), 1259–1271. doi:10.1016/j.ijggc.2011.07.001

Brady, P. V., and Walther, J. V. (1989). Controls on silicate dissolution rates in neutral and basic pH solutions at 25°C. *Geochim. Cosmochim. Acta* 53, 2823–2830. doi:10.1016/0016-7037(89)90160-9

Brigatti, M. F., Galan, E., and Theng, B. K. G. (2006). *Chapter 2 structures and mineralogy of clay minerals*. Elsevier. doi:10.1016/S1572-4352(05)01002-0

Cardona, A., Finkbeiner, T., and Santamarina, J. C. (2021). Natural rock fractures: From aperture to fluid flow. *Rock Mech. Rock Eng.* 54, 5827–5844. doi:10.1007/s00603-021-02565-1

Cartwright, J., James, D., and Bolton, A. (2003). The Genesis of polygonal fault systems: A review. *Geol. Soc. Lond. Spec. Publ.* 216, 223–243. doi:10.1144/GSL.SP.2003.216.01.15

Casey, W. H. (1991). On the relative dissolution rates of some oxide and orthosilicate minerals. *J. Colloid Interface Sci.* 146, 586–589. doi:10.1016/0021-9797(91)90225-W

Cha, M., and Santamarina, J. C. (2014). Dissolution of randomly distributed soluble grains: Post-dissolution k 0 -loading and shear. *Géotechnique* 64, 828–836. doi:10.1680/geot.14.P.115

Cha, M., and Santamarina, J. C. (2016). Hydro-chemo-mechanical coupling in sediments: Localized mineral dissolution. *Geomechanics Energy Environ.* 7, 1–9. doi:10.1016/j.gete.2016.06.001

Cha, M., and Santamarina, J. C. (2019). Localized dissolution in sediments under stress. *Granul. Matter* 21, 79–11. doi:10.1007/s10035-019-0932-4

Chiquet, P., Daridon, J. L., Broseta, D., and Thibeau, S. (2007). CO2/water interfacial tensions under pressure and temperature conditions of CO2 geological storage. *Energy Convers. Manag.* 48, 736–744. doi:10.1016/j.enconman.2006.09.011

Chun, B. S., and Wilkinson, G. T. (1995). Interfacial tension in high-pressure carbon dioxide mixtures. *Ind. Eng. Chem. Res.* 34, 4371–4377. doi:10.1021/ie00039a029

Correns, C. W. (1949). Growth and dissolution of crystals under linear pressure. *Discuss. Faraday Soc.* 5, 267. doi:10.1039/df9490500267

Crundwell, F. K. (2014). The mechanism of dissolution of minerals in acidic and alkaline solutions: Part I — a new theory of non-oxidation dissolution. *Hydrometallurgy* 149, 252–264. doi:10.1016/j.hydromet.2014.06.009

Da Rocha, S. R. P., Harrison, K. L., and Johnston, K. P. (1999). Effect of surfactants on the interfacial tension and emulsion formation between water and carbon dioxide. *Langmuir* 15, 419–428. doi:10.1021/la980844k

Daval, D., Hellmann, R., Saldi, G. D., Wirth, R., and Knauss, K. G. (2013). Linking nm-scale measurements of the anisotropy of silicate surface reactivity to macroscopic dissolution rate laws: New insights based on diopside. *Geochim. Cosmochim. Acta* 107, 121–134. doi:10.1016/j.gca.2012.12.045

de Gennes, P. G. (1985). Wetting: Statics and dynamics. *Rev. Mod. Phys.* 57 (3), 827–863. doi:10.1103/revmodphys.57.827

Demirel, Y. (2014). *Nonequilibrium thermodynamics: Transport and rate processes in physical, chemical and biological systems*. Elsevier. doi:10.1016/C2012-0-00459-0

Derr, N. J., Fronk, D. C., Weber, C. A., Mahadevan, A., Rycroft, C. H., and Mahadevan, L. (2020). Flow-driven branching in a frangible porous medium. *Phys. Rev. Lett.* 125, 158002. doi:10.1103/PhysRevLett.125.158002

DiCarlo, D. A. (2013). Stability of gravity-driven multiphase flow in porous media: 40 Years of advancements. *Water Resour. Res.* 49, 4531–4544. doi:10.1002/wrcr.20359

Dong, Z., Li, Y., Lin, M., and Li, M. (2013). A study of the mechanism of enhancing oil recovery using supercritical carbon dioxide microemulsions. *Pet. Sci.* 10, 91–96. doi:10.1007/s12182-013-0254-9

Drelich, J. W., Boinovich, L., Chibowski, E., Della Volpe, C., Hołysz, L., Marmur, A., et al. (2020). Contact angles: History of over 200 years of open questions. *Surf. Innov.* 8, 3–27. doi:10.1680/jsuin.19.00007

Duan, Z., and Sun, R. (2003). An improved model calculating CO2 solubility in pure water and aqueous NaCl solutions from 273 to 533 K and from 0 to 2000 bar. *Chem. Geol.* 193, 257–271. doi:10.1016/S0009-2541(02)00263-2

Duan, Z., Sun, R., Zhu, C., and Chou, I. M. (2006). An improved model for the calculation of CO2 solubility in aqueous solutions containing Na+, K+, Ca2+, Mg2+, Cl−, and SO42. *Mar. Chem.* 98 (2-4), 131–139. doi:10.1016/j.marchem.2005.09.001

Effenberger, H., Mereiter, K., and Zemann, J. (1981). Crystal structure refinements of magnesite, calcite, rhodochrosite, siderite, smithonite, and dolomite, with discussion of some aspects of the stereochemistry of calcite type carbonates. *Z. für Krist. - Cryst. Mat.* 156, 233–244. doi:10.1524/zkri.1981.156.14.233

Emami-Meybodi, H., Hassanzadeh, H., Green, C. P., and Ennis-King, J. (2015). Convective dissolution of CO2 in saline aquifers: Progress in modeling and experiments. *Int. J. Greenh. Gas Control* 40, 238–266. doi:10.1016/j.ijggc.2015.04.003

Eral, H. B., 't Mannetje, D. J. C. M., and Oh, J. M. (2013). Contact angle hysteresis: A review of fundamentals and applications. *Colloid Polym. Sci.* 291, 247–260. doi:10.1007/s00396-012-2796-6

Espinoza, D. N., Kim, S. H., and Santamarina, J. C. (2011). CO2 geological storage—geotechnical implications. *KSCE J. Civ. Eng.* 15 (4), 707–719. doi:10.1007/s12205-011-0011-9

Espinoza, D. N., and Santamarina, J. C. (2010). Water-CO2-mineral systems: Interfacial tension, contact angle, and diffusion - implications to CO2 geological storage. *Water Resour. Res.* 46, 1–10. doi:10.1029/2009WR008634

Espinoza, D. N., and Santamarina, J. C. (2012). Clay interaction with liquid and supercritical CO2: The relevance of electrical and capillary forces. *Int. J. Greenh. Gas Control* 10, 351–362. doi:10.1016/j.ijggc.2012.06.020

Espinoza, D. N., and Santamarina, J. C. (2017). CO2 breakthrough—caprock sealing efficiency and integrity for carbon geological storage. *Int. J. Greenh. Gas Control* 66, 218–229. doi:10.1016/j.ijggc.2017.09.019

Etheridge, M. A., Wall, V. J., Cox, S. F., and Vernon, R. H. (1984). High fluid pressures during regional metamorphism and deformation: Implications for mass transport and deformation mechanisms. *J. Geophys. Res.* 89, 4344–4358. doi:10.1029/JB089iB06p04344

Fischer, C., Arvidson, R. S., and Lüttge, A. (2012). How predictable are dissolution rates of crystalline material? *Geochim. Cosmochim. Acta* 98, 177–185. doi:10.1016/j.gca.2012.09.011

Fowler, A. C., and Yang, X. (1999). Pressure solution and viscous compaction in sedimentary basins. *J. Geophys. Res.* 104, 12989–12997. doi:10.1029/1998JB900029

Fredd, C. N. (2000). "Dynamic model of wormhole formation demonstrates conditions for effective skin reduction during carbonate matrix acidizing," in Proceeding of the SPE Permian Basin Oil Gas Recover. Conf. Proc., Midland, Texas, March 2000. doi:10.2118/59537-ms

Fredd, C. N., and Fogler, H. S. (1998). Alternative stimulation fluids and their impact on carbonate acidizing. *SPE J.* 3, 34–41. doi:10.2118/31074-PA

Freund, P., Bachu, S., and Gupta, M. (2006). Annex I - properties of CO2 and carbon-based fuels. *Carbon N. Y.*, 383–400.

Furrer, G., Zysset, M., and Schindler, P. W. (1993). "Weathering kinetics of montmorillonite: Investigations in batch and mixed-flow reactors," in *Geochemistry of clay-pore fluid interactions* (London: Chapman & Hall), 243–262.

Gachuz-Muro, H., and Sohrabi, M. (2013). "Effects of brine on crude oil viscosity at different temperature and brine composition - heavy oil/water interaction," in Proceeding of the 75th Eur. Assoc. Geosci. Eng. Conf. Exhib. 2013 Inc. SPE Eur. 2013 Chang. Front., London, UK, June 2013, 1878–1889. doi:10.2118/164910-ms

García, A. V. (2005). *Measurement and modelling of scaling minerals.*

García, A. V., Thomsen, K., and Stenby, E. H. (2005). Prediction of mineral scale formation in geothermal and oilfield operations using the extended UNIQUAC model. *Geothermics* 34, 61–97. doi:10.1016/j.geothermics.2004.11.002

Gauteplass, J., Almenningen, S., Barth, T., and Ersland, G. (2020). Hydrate plugging and flow remediation during CO2 injection in sediments. *Energies* 13, 4511. doi:10.3390/EN13174511

Gautier, J.-M., Oelkers, E. H., and Schott, J. (2001). Are quartz dissolution rates proportional to B.E.T. surface areas? *Geochim. Cosmochim. Acta* 65, 1059–1070. doi:10.1016/S0016-7037(00)00570-6

Georgiadis, A., Llovell, F., Bismarck, A., Blas, F. J., Galindo, A., Maitland, G. C., et al. (2010). Interfacial tension measurements and modelling of (carbon dioxide + n-alkane) and (carbon dioxide + water) binary mixtures at elevated pressures and temperatures. *J. Supercrit. Fluids* 55, 743–754. doi:10.1016/j.supflu.2010.09.028

Global status CCS (2021). *The global status of CCS 2021*. Australia.

Goldberg, R. N., and Parker, V. B. (1985). Thermodynamics of solution of SO2(g) in water and of aqueous sulfur dioxide solutions. *J. Res. Natl. Bur. Stand. (1977).* 90, 341. doi:10.6028/jres.090.024

Golfier, F., Zarcone, C., Bazin, B., Lenormand, R., Lasseux, D., and Quintard, M. (2002). On the ability of a Darcy-scale model to capture wormhole formation during the dissolution of a porous medium. *J. Fluid Mech.* 457, 213–254. doi:10.1017/S0022112002007735

Grandstaff, D. E. (1978). Changes in surface area and morphology and the mechanism of forsterite dissolution. *Geochim. Cosmochim. Acta* 42, 1899–1901. doi:10.1016/0016-7037(78)90245-4

Gu, Y., Hou, P., and Luo, W. (2013). Effects of four important factors on the measured minimum miscibility pressure and first-contact miscibility pressure. *J. Chem. Eng. Data* 58, 1361–1370. doi:10.1021/je4001137

Gysi, A. P., and Stefánsson, A. (2012). Experiments and geochemical modeling of CO2 sequestration during hydrothermal basalt alteration. *Chem. Geol.* 306307, 10–28. doi:10.1016/j.chemgeo.2012.02.016

Haghi, R. K., Chapoy, A., Peirera, L. M. C., Yang, J., and Tohidi, B. (2017). pH of CO2 saturated water and CO2 saturated brines: Experimental measurements and modelling. *Int. J. Greenh. Gas Control* 66, 190–203. doi:10.1016/j.ijggc.2017.10.001

Han, W. S., Stillman, G. A., Lu, M., Lu, C., McPherson, B. J., and Park, E. (2010). Evaluation of potential nonisothermal processes and heat transport during CO2 sequestration. *J. Geophys. Res.* 115, B07209. doi:10.1029/2009JB006745

Hayes, K. F., and Katz, L. E. (1996). "Application of X-ray absorption spectroscopy for surface complexation modelling of metal ion sorption," in *Physics and Chemistry of mineral surfaces*. Editor P. V. Brady (Baton Rouge): CRC Press), 147–223.

He, D., Xu, R., Ji, T., and Jiang, P. (2022). Experimental investigation of the mechanism of salt precipitation in the fracture during CO2 geological sequestration. *Int. J. Greenh. Gas Control* 118, 103693. doi:10.1016/j.ijggc.2022.103693

Hebach, A., Oberhof, A., Dahmen, N., Kögel, A., Ederer, H., and Dinjus, E. (2002). Interfacial tension at elevated pressures-measurements and correlations in the water + carbon dioxide system. *J. Chem. Eng. Data* 47, 1540–1546. doi:10.1021/je025569p

Hemmati-Sarapardeh, A., Ayatollahi, S., Ghazanfari, M. H., and Masihi, M. (2014). Experimental determination of interfacial tension and miscibility of the CO2-crude oil system; Temperature, pressure, and composition effects. *J. Chem. Eng. Data* 59, 61–69. doi:10.1021/je400811h

Hesse, M. A., Orr, F. M., and Tchelepi, H. A. (2008). Gravity currents with residual trapping. *J. Fluid Mech.* 611, 35–60. doi:10.1017/S002211200800219X

Hoteit, H., Fahs, M., and Soltanian, M. R. (2019). Assessment of CO2 injectivity during sequestration in depleted gas reservoirs. *Geosciences* 9 (5), 199. doi:10.3390/geosciences9050199

Houben, M., van Geijn, R., van Essen, M., Borneman, Z., and Nijmeijer, K. (2021). Supercritical CO2 permeation in glassy polyimide membranes. *J. Memb. Sci.* 620, 118922. doi:10.1016/j.memsci.2020.118922

Hough, E. W., Wood, B. B., and Rzasa, M. J. (1952). Adsorption at water–helium, –methane and –nitrogen interfaces at pressures to 15, 000 P.s.i.a. *J. Phys. Chem.* 56, 996–999. doi:10.1021/j150500a017

Hu, Y. F., and Guo, T. M. (2005). Effect of the structures of ionic liquids and alkylbenzene-derived amphiphiles on the inhibition of asphaltene precipitation from CO 2-injected reservoir oils. *Langmuir* 21, 8168–8174. doi:10.1021/la050212f

Huggins, M. L., and Sun, K.-H. (1946). Energy additivity in oxygen-containing crystals and glasses. *J. Phys. Chem.* 50, 319–328. doi:10.1021/j150448a003

Huhtamäki, T., Tian, X., Korhonen, J. T., and Ras, R. (2018). Surface-wetting characterization using contact-angle measurements. *Nat. Protoc.* 13, 1521–1538. doi:10.1038/s41596-018-0003-z

IPCC (2021). *IPCC*. Cambridge, United Kingdom: Cambridge Univ. Press. doi:10.1260/095830507781076194

Islam, A., Nia, K. A. K., Sepehrnoori, K., and Patzek, T. (2014). Effects of geochemical reaction on double diffusive natural convection of CO2 in brine saturated geothermal reservoir. *Energy Procedia* 63, 5357–5377. doi:10.1016/j.egypro.2014.11.568

James, L., Palandri, K., Yousif, K., and Kharaka, K. (2004). U.S. GEOLOGICAL SURVEY OPEN FILE REPORT (OF 2004-1068) National Energy Technology Laboratory. *Steve Jobs*. Menlo Park, NY: Department of Energy.

Jang, J., Narsilio, G. A., and Santamarina, J. C. (2011). Hydraulic conductivity in spatially varying media-a pore-scale investigation. *Geophys. J. Int.* 184 (3), 1167–1179. doi:10.1111/j.1365-246x.2010.04893.x

Jiang, L., Wang, S., Abudula, A., Liu, Y., and Song, Y. (2019). The effect of density difference on the development of density-driven convection under large Rayleigh number. *Int. J. Heat. Mass Transf.* 139, 1087–1095. doi:10.1016/j.ijheatmasstransfer.2019.05.027

Karnanda, W., Benzagouta, M. S., AlQuraishi, A., and Amro, M. M. (2013). Effect of temperature, pressure, salinity, and surfactant concentration on IFT for surfactant flooding optimization. *Arab. J. Geosci.* 6, 3535–3544. doi:10.1007/s12517-012-0605-7

Kiepe, J., Horstmann, S., Fischer, K., and Gmehling, J. (2002). Experimental determination and prediction of gas solubility data for CO2+H2O mixtures containing NaCl or KCl at temperatures between 313 and 393K and pressures up to 10 MPa. *Ind. Eng. Chem. Res.* 41 (17), 4393–4398. doi:10.1021/ie020154i

Kim, S., Espinoza, D. N., Jung, J., Cha, M., and Santamarina, J. C. (2019). "Carbon geological storage: Coupled processes, engineering and monitoring," in *Science of carbon storage in deep saline formations* (Elsevier), 383–407. doi:10.1016/B978-0-12-812752-0.00017-4

Kim, S., and Santamarina, J. C. (2014). Engineered CO2 injection: The use of surfactants for enhanced sweep efficiency. *Int. J. Greenh. Gas Control* 20, 324–332. doi:10.1016/j.ijggc.2013.11.018

Kim, S., and Santamarina, J. C. (2015). Reactive fluid flow in CO2 storage reservoirs: A 2-D pore network model study. *Greenh. Gas. Sci. Technol.* 5, 462–473. doi:10.1002/ghg.1487

Kim, S., and Santamarina, J. C. (2016). Geometry-coupled reactive fluid transport at the fracture scale: Application to CO 2 geologic storage. *Geofluids* 16 (2), 329–341. doi:10.1111/gfl.12152

Knauss, K. G., Nguyen, S. N., and Weed, H. C. (1993). Diopside dissolution kinetics as a function of pH, CO2, temperature, and time. *Geochim. Cosmochim. Acta* 57, 285–294. doi:10.1016/0016-7037(93)90431-U

Kneafsey, T. J., and Pruess, K. (2010). Laboratory flow experiments for visualizing carbon dioxide-induced, density-driven brine convection. *Transp. Porous Media* 82, 123–139. doi:10.1007/s11242-009-9482-2

Koschel, D., Coxam, J.-Y., Rodier, L., and Majer, V. (2006). Enthalpy and solubility data of CO2 in water and NaCl(aq) at conditions of interest for geological sequestration. *Fluid Phase Equilib.* 247 (1–2), 107–120. doi:10.1016/j.fluid.2006.06.006

Kvamme, B., Kuznetsova, T., Hebach, A., Oberhof, A., and Lunde, E. (2007). Measurements and modelling of interfacial tension for water + carbon dioxide systems at elevated pressures. *Comput. Mat. Sci.* 38, 506–513. doi:10.1016/j.commatsci.2006.01.020

Lahti, S. I., Raivio, P., and Laitakari, I. (2005). *Orbicular rocks in Finland, with contributions by paula raivio and ilkka laitakari*. Espoo: Geological Survey of Finland.

Lee, B. Y., and Kurtis, K. E. (2017). Effect of pore structure on salt crystallization damage of cement-based materials: Consideration of w/b and nanoparticle use. *Cem. Concr. Res.* 98, 61–70. doi:10.1016/j.cemconres.2017.04.002

Li, H., Yang, D., and Tontiwachwuthikul, P. (2012). Experimental and theoretical determination of equilibrium interfacial tension for the solvent(s)-CO 2-heavy oil systems. *Energy fuels.* 26, 1776–1786. doi:10.1021/ef201860f

Liesegang, R. E. (1896). Ueber einige Eigenschaften von Gallerten. *Naturwissenschaftliche. Wochenschrift* 11, 353.

Liu, Q., and Santamarina, J. C. (2022). Fluid- driven instabilities in granular media: From viscous fingering and dissolution wormholes to desiccation cracks and ice lenses. *Front. Mech. Eng.* 8, 861554. doi:10.3389/fmech.2022.861554

Maliva, R. G., and Siever, R. (1988). Mechanism and controls of silicification of fossils in limestones. *J. Geol.* 96, 387–398. doi:10.1086/629235

Markham, A. E., and Kobe, K. A. (1941). The solubility of carbon dioxide in aqueous solutions of sulfuric and perchloric acids at 25°. *J. Am. Chem. Soc.* 63, 1165–1166. doi:10.1021/ja01849a507

Menke, H. P., Bijeljic, B., and Blunt, M. J. (2017). Dynamic reservoir-condition microtomography of reactive transport in complex carbonates: Effect of initial pore structure and initial brine pH. *Geochim. Cosmochim. Acta* 204, 267–285. doi:10.1016/j.gca.2017.01.053

Miri, R., Aagaard, P., and Hellevang, H. (2014). Examination of CO2 –so 2 solubility in water by SAFT1. Implications for CO2 transport and storage. *J. Phys. Chem. B* 118, 10214–10223. doi:10.1021/jp505562j

Miri, R., van Noort, R., Aagaard, P., and Hellevang, H. (2015). New insights on the physics of salt precipitation during injection of CO2 into saline aquifers. *Int. J. Greenh. Gas Control* 43, 10–21. doi:10.1016/j.ijggc.2015.10.004

Mullins, O. C. (2010). The modified yen model. *Energy fuels.* 24, 2179–2207. doi:10.1021/ef900975e

Nabika, H., Itatani, M., and Lagzi, I. (2020). Pattern formation in precipitation reactions: The Liesegang phenomenon. *Langmuir* 36, 481–497. doi:10.1021/acs.langmuir.9b03018

Nakhaei-Kohani, R., Taslimi-Renani, E., Hadavimoghaddam, F., Mohammadi, M.-R., and Hemmati-Sarapardeh, A. (2022). Modeling solubility of CO2–N2 gas mixtures in aqueous electrolyte systems using artificial intelligence techniques and equations of state. *Sci. Rep.* 12, 3625. doi:10.1038/s41598-022-07393-z

National Academies of Sciences Engineering and Medicine (2020). *Characterization, modeling, monitoring, and remediation of fractured rock*. Washington, DC: The National Academies Press. doi:10.17226/21742

Ng, K., and Santamarina, J. C. (2022). Mechanical and hydraulic properties of carbonate rocks - the critical role of porosity. *J. Rock Mech. Geotech. Eng.* doi:10.1016/j.jrmge.2022.07.017

NIST Chemistry WebBook (2022). *NIST stand. Ref. Database number 69.*

Nobakht, M., Moghadam, S., and Gu, Y. (2008). Mutual interactions between crude oil and CO2 under different pressures. *Fluid Phase Equilib.* 265, 94–103. doi:10.1016/j.fluid.2007.12.009

O'Connor, W. K., Dahlin, D. C., Nilsen, D. N., Rush, G. E., and WaltersRichard P Turner, P. C. (2001). "Carbon dioxide sequestration by direct mineral carbonation: Results from recent studies and current status," in *First national conference on carbon sequestration* (Washington, DC.

O'Connor, W. K., Dahlin, D. C., Rush, G. E., Dahlin, C. L., and Collins, W. K. (2002). Carbon dioxide sequestration by direct mineral carbonation: Process mineralogy of feed and products. *Min. Metall. Explor.* 19, 95–101. doi:10.1007/BF03403262

Oelkers, E. H., Declercq, J., Saldi, G. D., Gislason, S. R., and Schott, J. (2018). Olivine dissolution rates: A critical review. *Chem. Geol.* 500, 1–19. doi:10.1016/j.chemgeo.2018.10.008

Oldenburg, C. M. (2007). Joule-Thomson cooling due to CO2 injection into natural gas reservoirs. *Energy Convers. Manag.* 48, 1808–1815. doi:10.1016/j.enconman.2007.01.010

Palandri, J. L., and Kharaka, Y. K. (2004). *A compilation of rate parameters of water-mineral interaction kinetics for application to geochemical modeling*. Open-File Report. USGS Numbered S.

Panjarian, S., and Sultan, R. (2001). Crystal selection and Liesegang banding in dynamic precipitate systems. *Collect. Czechoslov. Chem. Commun.* 66, 541–554. doi:10.1135/cccc20010541

Park, J. Y., Lim, J. S., Yoon, C. H., Lee, C. H., and Park, K. P. (2005). Effect of a fluorinated sodium bis(2-ethylhexyl) sulfosuccinate (aerosol-OT, AOT) analogue surfactant on the interfacial tension of CO 2 + water and CO2 + Ni-plating solution in near- and supercritical CO2. *J. Chem. Eng. Data* 50, 299–308. doi:10.1021/je0499667

Peng, C., Crawshaw, J. P., Maitland, G. C., Martin Trusler, J. P., and Vega-Maza, D. (2013). The pH of CO2-saturated water at temperatures between 308 K and 423 K at pressures up to 15 MPa. *J. Supercrit. Fluids* 82, 129–137. doi:10.1016/j.supflu.2013.07.001

Phuoc, T. X., and Massoudi, M. (2021). Using CO2 as a cooling fluid for power plants: A novel approach for CO2 storage and utilization. *Appl. Sci. (Basel).* 11, 4974. doi:10.3390/APP11114974

Pokrovsky, O. S., Golubev, S. V., and Schott, J. (2005). Dissolution kinetics of calcite, dolomite and magnesite at 25 °C and 0 to 50 atm pCO2. *Chem. Geol.* 217, 239–255. doi:10.1016/j.chemgeo.2004.12.012

Pollet-Villard, M., Daval, D., Ackerer, P., Saldi, G. D., Wild, B., Knauss, K. G., et al. (2016). Does crystallographic anisotropy prevent the conventional treatment of aqueous mineral reactivity? A case study based on K-feldspar dissolution kinetics. *Geochim. Cosmochim. Acta* 190, 294–308. doi:10.1016/j.gca.2016.07.007

Rácz, Z. (1999). formation of Liesegang patterns. *Phys. A Stat. Mech. its Appl.* 274, 50–59. doi:10.1016/S0378-4371(99)00432-X

Rezk, M. G., and Foroozesh, J. (2019). Phase behavior and fluid interactions of a CO2-Light oil system at high pressures and temperatures. *Heliyon* 5, e02057. doi:10.1016/j.heliyon.2019.e02057

Rutter, E. H. (1983). Pressure solution in nature, theory and experiment. *J. Geol. Soc. Lond.* 140, 725–740. doi:10.1144/gsjgs.140.5.0725

Sanaei, A., Varavei, A., and Sepehrnoori, K. (2019). Mechanistic modeling of carbonated waterflooding. *J. Pet. Sci. Eng.* 178, 863–877. doi:10.1016/j.petrol.2019.04.001

Sargent, J. P., Tredwell, S., Dixon, D. G., Buxton, A. L., Shanahan, M. E. R., Padday, J. F., et al. (2005). *Handbook of adhesion*. Chichester, UK: John Wiley & Sons, 579–620. doi:10.1002/0470014229.ch21

Savary, V., Berger, G., Dubois, M., Lacharpagne, J.-C., Pages, A., Thibeau, S., et al. (2012). The solubility of CO2+H2S mixtures in water and 2M NaCl at 120°C and pressures up to 35MPa. *Int. J. Greenh. Gas Control* 10, 123–133. doi:10.1016/j.ijggc.2012.05.021

Schmelzer, J. W. P., Zanotto, E. D., and Fokin, V. M. (2005). Pressure dependence of viscosity. *J. Chem. Phys.* 122, 074511. doi:10.1063/1.1851510

Schmid, R. (2001). Recent advances in the description of the structure of water, the hydrophobic effect, and the like-dissolves-like rule. *Monatsh. fur Chem.* 132, 1295–1326. doi:10.1007/s007060170019

Schott, J., Berner, R. A., and Sjöberg, E. L. (1981). Mechanism of pyroxene and amphibole weathering—I. Experimental studies of iron-free minerals. *Geochim. Cosmochim. Acta* 45, 2123–2135. doi:10.1016/0016-7037(81)90065-X

Schott, J., and Berner, R. A. (1983). X-ray photoelectron studies of the mechanism of iron silicate dissolution during weathering. *Geochim. Cosmochim. Acta* 47, 2233–2240. doi:10.1016/0016-7037(83)90046-7

Shafabakhsh, P., Ataie-Ashtiani, B., Simmons, C. T., Younes, A., and Fahs, M. (2021). Convective-reactive transport of dissolved CO2 in fractured-geological formations. *Int. J. Greenh. Gas Control* 109, 103365. doi:10.1016/j.ijggc.2021.103365

Shin, H., Santamarina, J. C., and Cartwright, J. A. (2008). Contraction-driven shear failure in compacting uncemented sediments. *Geol.* 36, 931. doi:10.1130/G24951A.1

Shin, H., Santamarina, J. C., and Cartwright, J. A. (2010). Displacement field in contraction-driven faults. *J. Geophys. Res.* 115, B07408. doi:10.1029/2009JB006572

Shin, H., and Santamarina, J. C. (2010). Fluid-driven fractures in uncemented sediments: Underlying particle-level processes. *Earth Planet. Sci. Lett.* 299 (1-2), 180–189. doi:10.1016/j.epsl.2010.08.033

Shin, H., and Santamarina, J. C. (2009). Mineral dissolution and the evolution of k0. *J. Geotech. Geoenviron. Eng.* 135, 1141–1147. doi:10.1061/(ASCE)GT.1943-5606.0000053

Shin, H., and Santamarina, J. C. (2011). Open-mode discontinuities in soils. *Geotech. Lett.* 1, 95–99. doi:10.1680/geolett.11.00014

Simeoni, G. G., Bryk, T., Gorelli, F. A., Krisch, M., Ruocco, G., Santoro, M., et al. (2010). The Widom line as the crossover between liquid-like and gas-like behaviour in supercritical fluids. *Nat. Phys.* 6, 503–507. doi:10.1038/nphys1683

Simon, R., and Graue, D. J. (1965). Generalized correlations for predicting solubility, swelling and viscosity behavior of CO2 -crude oil systems. *J. Pet. Technol.* 17, 102–106. doi:10.2118/917-pa

Sloan, E. D. (2010). *Natural gas hydrates in flow assurance*. Burlington, MA: Gulf Professional Publishing. doi:10.1016/C2009-0-62311-4

Snæbjörnsdóttir, S. Ó., Gislason, S. R., Galeczka, I. M., and Oelkers, E. H. (2018). Reaction path modelling of *in-situ* mineralisation of CO2 at the CarbFix site at Hellisheidi, SW-Iceland. *Geochim. Cosmochim. Acta* 220, 348–366. doi:10.1016/j.gca.2017.09.053

Snæbjörnsdóttir, S. Ó., Sigfússon, B., Marieni, C., Goldberg, D., Gislason, S. R., and Oelkers, E. H. (2020). Carbon dioxide storage through mineral carbonation. *Nat. Rev. Earth Environ.* 1, 90–102. doi:10.1038/s43017-019-0011-8

Stumm, W., and Morgan, J. J. (1996). Aquatic Chemistry, Chemical Equilibria and Rates in Natural Waters. *J. Chem. Educ.* 3rd Edn. New York: 73.

Sutjiadi-Sia, Y., Jaeger, P., and Eggers, R. (2008). Interfacial phenomena of aqueous systems in dense carbon dioxide. *J. Supercrit. Fluids* 46, 272–279. doi:10.1016/j.supflu.2008.06.001

Sverdrup, H. U. (1990). *The kinetics of base cation release due to chemical weathering*. Lund, Sweden: Lund University Press.

Taber, S. (1916). The growth of crystals under external pressure. *Am. J. Sci.* s4-41, 532–556. doi:10.2475/ajs.s4-41.246.532

Talman, S., Shokri, A. R., Chalaturnyk, R., and Nickel, E. (2020). "Salt precipitation at an active CO2 injection site," in *Gas injection into geological formations and related topics* (John Wiley & Sons), 183–199. doi:10.1002/9781119593324.ch11

Van der Meer, L. G. H. (1993). The conditions limiting CO2 storage in aquifers. *Energy Convers. Manag.* 34, 959–966. doi:10.1016/0196-8904(93)90042-9

Velbel, M. A. (1999). Bond strength and the relative weathering rates of simple orthosilicates. *Am. J. Sci.* 299, 679–696. doi:10.2475/ajs.299.7-9.679

Verma, M. K. (2015). *Fundamentals of carbon dioxide-enhanced oil recovery (CO2-EOR): A supporting document of the assessment methodology for hydrocarbon recovery using CO2-EOR associated with carbon sequestration*. Washington, DC: US Department of the Interior, US Geological Survey, 19.

Vilarrasa, V., Rinaldi, A. P., and Rutqvist, J. (2017). Long-term thermal effects on injectivity evolution during CO2 storage. *Int. J. Greenh. Gas Control* 64, 314–322. doi:10.1016/j.ijggc.2017.07.019

Vilarrasa, V., and Rutqvist, J. (2017). Thermal effects on geologic carbon storage. *Earth. Sci. Rev.* 165, 245–256. doi:10.1016/j.earscirev.2016.12.011

Wang, X., Zhang, S., and Gu, Y. (2010). Four important onset pressures for mutual interactions between each of three crude oils and CO2. *J. Chem. Eng. Data* 55, 4390–4398. doi:10.1021/je1005664

Wiltschko, D. V., and Morse, J. W. (2001). Crystallization pressure versus "crack seal" as the mechanism for banded veins. *Geology* 29, 79. doi:10.1130/0091-7613(2001)029<0079:CPVCSA>2.0.CO;2

Xie, Z. (1994). *Surface properties of silicates, their stability and dissolution kinetics*.

Xiong, W., Wells, R. K., Horner, J. A., Schaef, H. T., Skemer, P. A., and Giammar, D. E. (2018). CO 2 mineral sequestration in naturally porous basalt. *Environ. Sci. Technol. Lett.* 5, 142–147. doi:10.1021/acs.estlett.8b00047

Yasunishi, A., and Yoshida, F. (1979). Solubility of carbon dioxide in aqueous electrolyte solutions. *J. Chem. Eng. Data* 24, 11–14. doi:10.1021/je60080a007

Young, T. (1805). III. An essay on the cohesion of fluids. *Philos. Trans. R. Soc. Lond.* 95, 65–87. doi:10.1098/rstl.1805.0005

Zhang, H. (1990). *Factors determining the rate and stoichiometry of hornblende dissolution*.

Zheng, C., Brunner, M., Li, H., Zhang, D., and Atkin, R. (2019). Dissolution and suspension of asphaltenes with ionic liquids. *Fuel* 238, 129–138. doi:10.1016/j.fuel.2018.10.070

Zolghadr, A., Escrochi, M., and Ayatollahi, S. (2013). Temperature and composition effect on CO2 miscibility by interfacial tension measurement. *J. Chem. Eng. Data* 58, 1168–1175. doi:10.1021/je301283e

Glossary

a_{H^+} [] Activity of protons

c [mol/l] Solute concentration (0: at saturation)

$\boldsymbol{C_p}$ **[J/K]** Heat capacity

D [m²/s] Molecular diffusion coefficient

$\boldsymbol{d^*}$ **[m]** Characteristic pore diameter

Da [] Damköhler number

e [] Void ratio

E [GPa] Young's modulus

g **[m/s]** Gravitational acceleration

H **[m]** Height of the fluid column (CO_2: carbon dioxide column; R: reservoir)

k [mol m^{-2} s^{-1}] Rate constant of mineral dissolution

$\boldsymbol{k_0}$ [] Lateral coefficient earth pressure (0: at rest; a: Rankine's active case)

$\boldsymbol{k_H}$ **[mol L^{-1} atm^{-1}]** Henry's constant

$\mathbf{k}_{\boldsymbol{hyd}}$ **[m²]** Permeability

$\boldsymbol{L_{ch}}$ **[m]** Channel length

$\boldsymbol{l_0}$ **[m]** Intermolecular distance

M **[g/mol]** Molar mass (CO_2; silic: silicate minerals)

n_{H^+} [] Reaction order with respect to the activity of protons

P **[Pa]** Pressure (0: initial pressure; CO_2: partial pressure CO_2; nw: non-wetting fluid; w: wetting fluid; crys: on a growing crystal; sol: solution)

Pe [] Péclet number

R **[J mol^{-1} K^{-1}]** Gas constant

Ra [] Rayleigh number

r **[m]** Radius of the interface

$\boldsymbol{r_d}$ **[mol/s]** Mineral dissolution rate

S [] Supersaturation

s **[m²]** Surface area

$\boldsymbol{S_s}$ **[m²/g]** Specific surface area

$\boldsymbol{S_w}$ [] Degree of water saturation

SD **[kg/m³]** Storage density in terms of kg of CO_2 per m³ of the reservoir

T **[K]** Absolute temperature

$\boldsymbol{T_p}$ **[m]** Plume thickness

t **[s]** Time (adv: advection; diff: diffusion; r: reactive)

$\boldsymbol{V_m}$ **[m³/mol]** Mineral molar volume

v **[m/s]** Average flow velocity

z [m] Height of the sediment column

$\mathbf{z_w}$ **[m]** Height of the water column above the seafloor

$\boldsymbol{\alpha}$ **[K^{-1}]** The coefficient of thermal expansion

$\boldsymbol{\beta}$ [] Factor related to the pore size distribution

$\boldsymbol{\gamma}$ **[N/m]** Interfacial tension (FS: fluid-solid; LS: liquid-solid; LF: fluid-liquid)

$\boldsymbol{\Delta H}$ **[kJ/kg]** Enthalpy change in phase transformation

$\boldsymbol{\varepsilon}$[] Strain

$\boldsymbol{\theta}$ [°] Contact angle (A: advancing; R: receding)

$\boldsymbol{\kappa}$ **[1/s]** Kinetic rate of mineral dissolution

$\boldsymbol{\mu}$ **[μPa·s]** Fluid Viscosity (w: water)

$\boldsymbol{\mu_{JT}}$ [] Joule-Thomson coefficient

$\boldsymbol{\Pi_{seal}}$ [] Dimensionless ratio (seal: sealing number; stability: stability number)

$\boldsymbol{\rho}$ **[kg/m³]** Density (b: bulk; CO_2; hyd: hydrate; m: mineral; W: water; 0: initial fluid density)

$\boldsymbol{\sigma'}$ **[Pa]** Effective stress (h: horizontal; v: vertical; z_0: under zero lateral strain conditions)

$\boldsymbol{\chi_{CO2}}$ **[mol/L]** Solubility of CO_2

$\boldsymbol{\varphi}$ [] Porosity

ψ [] Geometric fabric factor